ARMY RESEARCH LABORATORY

Numerical Computations of Supersonic Flow Over a Square Cross-Section Missile

by Sidra I. Silton and Jubaraj Sahu

ARL-TR-3562 **August 2005**

NOTICES

Disclaimers

The findings in this report are not to be construed as an official Department of the Army position unless so designated by other authorized documents.

Citation of manufacturer's or trade names does not constitute an official endorsement or approval of the use thereof.

Destroy this report when it is no longer needed. Do not return it to the originator.

Army Research Laboratory
Aberdeen Proving Ground, MD 21005-5066

ARL-TR-3562 **August 2005**

Numerical Computations of Supersonic Flow Over a Square Cross-Section Missile

Sidra I. Silton and Jubaraj Sahu
Weapons and Materials Research Directorate, ARL

REPORT DOCUMENTATION PAGE	Form Approved OMB No. 0704-0188

1. REPORT DATE *(DD-MM-YYYY)*	2. REPORT TYPE	3. DATES COVERED (From - To)
August 2005	Final	June 2002 –March 2004

4. TITLE AND SUBTITLE
Numerical Computations of Supersonic Flow Over a Square Cross-Section Missile

5a. CONTRACT NUMBER

5b. GRANT NUMBER

5c. PROGRAM ELEMENT NUMBER

6. AUTHOR(S)
Sidra I. Silton and Jubaraj Sahu

5d. PROJECT NUMBER
622617.H8000

5e. TASK NUMBER

5f. WORK UNIT NUMBER

7. PERFORMING ORGANIZATION NAME(S) AND ADDRESS(ES)
U.S. Army Research Laboratory
ATTN: AMSRD-ARL-WM-BC
Aberdeen Proving Ground, MD 21005-5066

8. PERFORMING ORGANIZATION REPORT NUMBER
ARL-TR-3562

9. SPONSORING/MONITORING AGENCY NAME(S) AND ADDRESS(ES)
The Technical Cooperation Program
TTCP KTA2-19

10. SPONSOR/MONITOR'S ACRONYM(S)

11. SPONSOR/MONITOR'S REPORT NUMBER(S)

12. DISTRIBUTION/AVAILABILITY STATEMENT
Approved for public release; distribution is unlimited.

13. SUPPLEMENTARY NOTES

14. ABSTRACT
This report describes a computational study undertaken to determine the aerodynamics of a nonaxisymmetric missile with a square cross section. Numerical solutions have been obtained at supersonic speeds for various roll orientations and angles of attack using a two-equation Reynolds-averaged Navier-Stokes turbulence model. Numerical results show the qualitative features (vortices and cross-flow separation regions) of the flow field at various stream wise positions along the missile configurations. Aerodynamic coefficients have been obtained from the computed solutions and found to match well with the available experimental data for these configurations. These numerical results show the ability of computational fluid dynamics techniques to accurately predict the aerodynamics of nonaxisymmetric missiles with a square cross section.

15. SUBJECT TERMS
nonaxisymmetric missile, complex flows, computational fluid dynamics

16. SECURITY CLASSIFICATION OF:			17. LIMITATION OF ABSTRACT	18. NUMBER OF PAGES	19a. NAME OF RESPONSIBLE PERSON
a. REPORT	b. ABSTRACT	c. THIS PAGE			Sidra I. Silton
UNCLASSIFIED	UNCLASSIFIED	UNCLASSIFIED	UL	52	19b. TELEPHONE NUMBER (*Include area code*) 410-278-7782

Contents

List of Figures

List of Tables

Acknowledgments

This work was accomplished as part of The Technical Cooperation Program between the United States, Canada, United Kingdom, and Australia on Weapons Technical Panel TP-2 Key Technology Area 2-19. The authors wish to thank Sukumar Chakravarthy from Metacomp Technologies for his expert technical advice. This work was supported by a grant of computer time from the Department of Defense High Performance Computing Major Shared Resource Center at the U.S. Army Research Laboratory.

INTENTIONALLY LEFT BLANK.

1. Introduction

The prediction of aerodynamic coefficients for projectile configurations is essential in assessing the performance of new designs. Accurate determination of aerodynamics is critical to the low-cost development of new advanced guided projectiles, rockets, missiles, and smart munitions. Fins, canards, and jets can be used to provide control for maneuvering projectiles and missiles. The flow fields associated with these control mechanisms for the modern weapons are complex, involving three-dimensional (3-D) shock-boundary layer interactions and highly viscous dominated separated flow regions (*1*–*3*). Computational fluid dynamics (CFD) has emerged as a critical technology for the aerodynamic design and assessment of weapons. Improved computer technology and state-of-the-art numerical procedures enable solutions to complex, 3-D problems associated with projectile and missile aerodynamics. In general, these techniques produce accurate and reliable numerical results for simple projectile and missile configurations at small angles of attack.

Modern weapons and the associated flow fields have increased in complexity as a result of changing military requirements. An increasing number of new weapon configurations are beyond the scope of traditional engineering prediction methods. Modern projectiles and missiles are expected to experience moderate to large angles of attack during flight. The flow field surrounding a slender missile at incidence features flow separations both from smooth bodies and sharp-edged lifting and control surfaces. Body and wing vortices (*4*, *5*) can dominate the flow field and interact with one another resulting in a very complex flow field even for simple geometries. Earlier work (*6*, *7*) on modeling of high angle of attack flow fields for finned missile configurations was initiated as part of The Technical Cooperation Program (TTCP) effort with participants from Canada, the United Kingdom, Australia, and the United States. This study addressed the application of Navier-Stokes methods to the prediction of flows around finned missile configurations and assessed the capabilities of Navier-Stokes solvers for the prediction of missile flow field at moderate to high angles of attack. It promoted technical interchange between aerodynamics specialists in the areas of grid generation, algorithms, turbulence modeling, and flow field visualization. The results of this study were reported in a special session of the AIAA Applied Aerodynamics Conference held in Denver, CO in August 2000 (*6*–*8*). The study has shown that all Navier-Stokes methods employed were capable of providing accurate predictions of the overall normal force and pitching moment characteristics, even at very high angles of attack. However, some significant discrepancies in the prediction of the axial force were evident. In general, the agreement between computed and measured flow fields was good. Higher order turbulence models such as the k-ε models did not provide better accuracy compared to simpler algebraic and one-equation models. The next phase of the research was to extend the scope of that study and to undertake a follow-on study to apply CFD

technology to the prediction of aerodynamic flow fields for nonaxisymmetric missile configurations.

Maneuvering nonaxisymmetric missile configurations can be used for increased lethality and are being explored for future weapon systems in various scenarios. Additionally, nonaxisymmetric projectiles have been shown to generate large amounts of lift compared to conventional circular projectiles (*9*). The aerodynamics of such configurations at high speeds are quite complex due to strong cross-flow influences and flow separation. Of particular interest was the accurate determination of supersonic and hypersonic flow over elliptic projectiles at moderate angles of attack. The flow field for such projectiles with nonaxisymmetric cross sections is complex, especially in the presence of jets used to maneuver these projectiles. This work, initiated as part of another TTCP effort with participants from Canada, the United Kingdom, and the United States, was aimed at assessing the capabilities of the both Euler and Navier-Stokes solvers currently available to research scientists for supersonic flow over elliptic projectiles for both jet-off and jet-on conditions (*10*, *11*). The TTCP research effort also included wind-tunnel testing and free-flight testing of these projectiles. CFD approaches that included both Euler and Navier-Stokes schemes, structured and unstructured techniques, and a variety of turbulence models were used in the numerical simulations (*10*, *11–15*). In general, very good agreement of the computed aerodynamic coefficients with the experimental data was achieved at all angles of attack investigated for the jet-off uncontrolled conditions. Accurate prediction of the jet-on cases was found to be a little more challenging than the jet-off cases (*16*). The results of this study were reported in a special session of the AIAA Atmospheric Flight Mechanics Conference held in Montreal, Canada in August 2001.

The TTCP efforts have continued recently with a focus on the application of CFD to missile aerodynamics which takes it to the next level of difficulty, that of multiple sets of fins on a elliptic cross-section missile. An additional nonaxisymmetric configuration was also investigated. Again, the objective here is to compare the results obtained from Navier-Stokes computations against experimental data, evaluate the accuracy of the predictive technologies, and identify priorities for future development. The present research focuses on the application of advanced CFD techniques for accurate numerical prediction of supersonic flow over two nonaxisymmetric missile configurations, one with a square cross section and the other with an elliptic cross section; both have multiple sets of complex fins. Numerical computations for these complex configurations have been performed at supersonic speeds and for several angles of attack. Only the results of the square cross-section axisymmetric missile configuration are presented in this report.

A description of the computational techniques is presented, followed by a description of the applications of these techniques to the square section configurations. Computed results for these configurations are presented at Mach 2.5 and 4.5 and several angles of attack from 0° to 20°. Computed data have been compared with experimental data provided by the Defence Science

and Technology Laboratory (DSTL, formerly the Defence Evaluation and Research Agency of the United Kingdom) (*17*).

2. Solution Technique

A commercially available code, CFD++ (*18*, *19*), is used for the CFD simulations. The basic numerical framework in the code contains unified-grid, unified-physics, and unified-computing features. A brief synopsis of this framework and methodology is given in the following paragraphs. The user is referred to the previous references for details.

The 3-D, Reynolds-averaged Navier-Stokes (*20*) equations are solved using the following finite volume method:

$$\frac{\partial}{\partial t}\int_{v}\mathbf{W}dV+\oint\left[\mathbf{F}-\mathbf{G}\right]\cdot dA=\int_{v}\mathbf{H}dV \quad , \tag{1}$$

where **W** is the vector of conservative variables, **F** and **G** are the inviscid and viscous flux vectors, respectively, **H** is the vector of source terms, V is the cell volume, and A is the surface area of the cell face.

The numerical framework of CFD++ is based on the following general elements:

1. unsteady compressible and incompressible Navier-Stokes equations with turbulence modeling (unified physics),
2. unification of Cartesian, structured curvilinear, and unstructured grids, including hybrids (unified grid),
3. unification of treatment of various cell shapes including hexahedral, tetrahedral, and triangular prism cells 3-D, quadrilateral and triangular cells two dimensional, and linear elements one-dimensional (unified grid),
4. treatment of multiblock patched aligned (nodally connected), patched-nonaligned, and overset grids (unified grid),
5. total Variation Diminishing discretization based on a new multidimensional interpolation framework,
6. Riemann solvers to provide proper signal propagation physics, including versions for preconditioned forms of the governing equations,
7. consistent and accurate discretization of viscous terms using the same multidimensional polynomial framework,

8. pointwise turbulence models that do not require knowledge of distance to walls,
9. versatile boundary condition implementation including a rich variety of integrated boundary condition types for the various sets of equations, and
10. implementation on massively parallel computers based on the distributed-memory message-passing model using native message-passing libraries or MPI, PVM, etc. (unified computing).

The code has brought together several ideas on convergence acceleration to yield a fast methodology for all flow regimes. The approach can be labeled as a "preconditioned-implicit-relaxation" scheme. It combines three basic ideas: implicit local time-stepping, relaxation, and preconditioning. Preconditioning the equations ideally equalizes the eigenvalues of the inviscid flux Jacobians and removes the stiffness arising from large discrepancies between the flow and sound velocities at low speeds. Use of an implicit scheme circumvents the stringent stability limits suffered by their explicit counterparts, and successive relaxation allows update of cells as information becomes available and thus aids convergence.

Second-order discretization was used for the flow variables and the turbulent viscosity equation. Turbulence closure is based on topology-parameter-free formulations. The realizable k-ε turbulence model (*21*) was used for the computation of turbulent flows for the missile configurations considered here. The next section describes the model geometries and the flow conditions for the square-section missile (*17*).

3. Model Geometry and Flowfield Conditions

3.1 Model Geometry

Two configurations were utilized for the square-section missile (*17*)—corner fins and side fins. The nose and body of the configurations were the same for each configuration (figure 1). The nose is 340.36 mm long and transitions from a pointed ogive to a square cross section. The remainder of the projectile has a square cross section (93.98 mm on a side) for a total projectile length of 1221.74 mm. All moments are referenced from the nose and are positive in the direction indicated in figure 1.

The fin geometry, an elongated pyramid, was the same for each configuration (figure 2). The root chord was 74.42 mm, with the leading edge of the fin placed 1040.13 mm from the nose tip. Each fin was 74.42 mm high and had a sweep angle of 45°. The fin had a taper angle of 6.83° with a maximum thickness of 7.87 mm. The only difference between the two configurations was the circumferential placement of the fins on the body. For the corner fin configuration, the fin tip of each fin was placed on the edge of the square (figure 3). For the side fin configuration, the fin tip of each fin was placed on the centerline of one side of the square (figure 4).

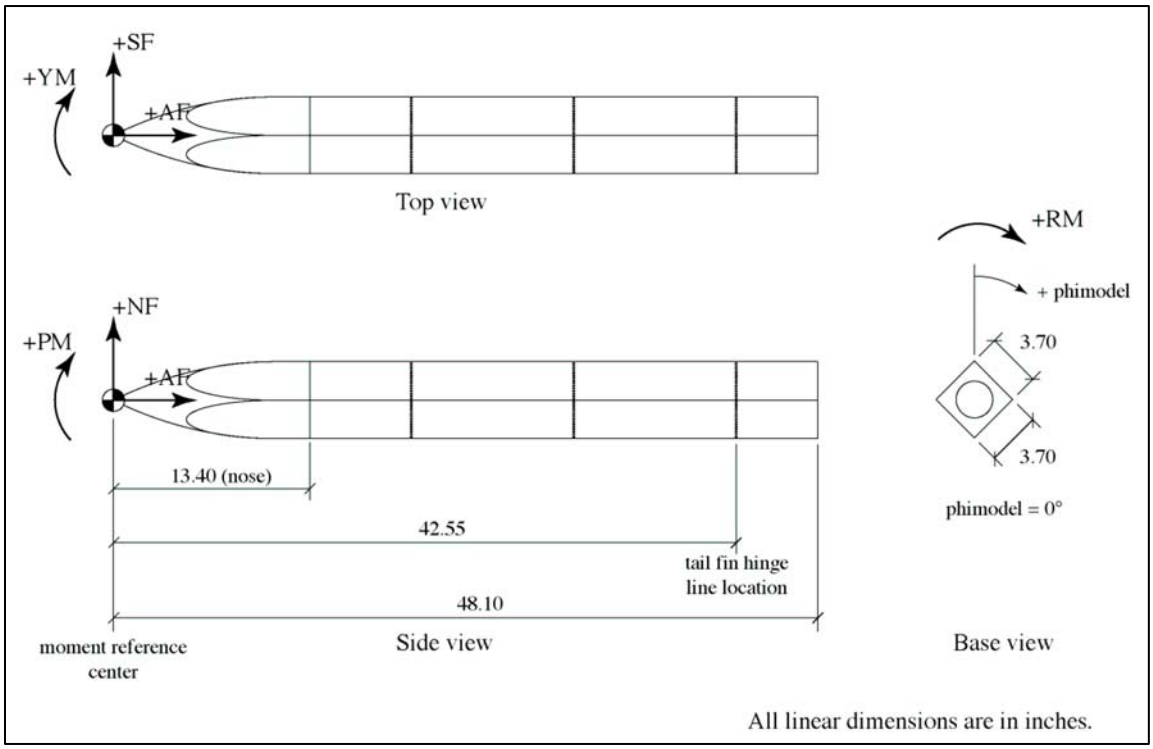

Figure 1. Reference dimensions and orientation for the square section missile, no fins.

3.2 Numerical Grid

Four unstructured grids were created, two for each geometry, using ICEM CFD (*22*). For the corner fin configuration, a grid containing 9.9 million hexahedral cells and 30,000 triangular prisms was constructed to have a y^+ of ~30 (figure 5). A second, more efficiently constructed grid containing 6.2 million hexahedral cells was constructed to have a y^+ of ~1.0 (figure 6). For the side fin configuration, both grids were constructed with a y^+ of ~1.0, but had different cell distributions. The resulting grids had 6.7 million and 9.0 million hexahedral cells (figure 7), respectively. A grid resolution study was completed between these grids and is presented in section 4.1.

3.3 Flowfield Conditions

A series of computations at both Mach 2.5 and Mach 4.5 was performed for each geometry at 14° angle of attack for roll orientations of 0°, 22.5°, and 45° (figure 8). An additional computational series was performed at Mach 2.5 for the side fin configuration at 20° angle of attack for the 0° roll orientation. These computations were completed in the blind as the experimental test was conducted concurrently. In order to accurately compare the CFD results to the experimental results after they became available, wind tunnel Reynolds number, Re, stagnation temperature, T_0, and stagnation pressure, P_0, were matched; Re = 1.31×10^7 per meter for both Mach 2.5 and 4.5, T_0 = 324.82 K and P_0 = 153.22 kPa for Mach 2.5, and T_0 = 338.71 K and P_0 = 446.83 kPa for Mach 4.5. These conditions correspond to static temperatures and pressures of 144.36 K and 8.92 kPa, respectively, at Mach 2.5 and 67.07 K and 1.54 kPa, respectively, at Mach 4.5.

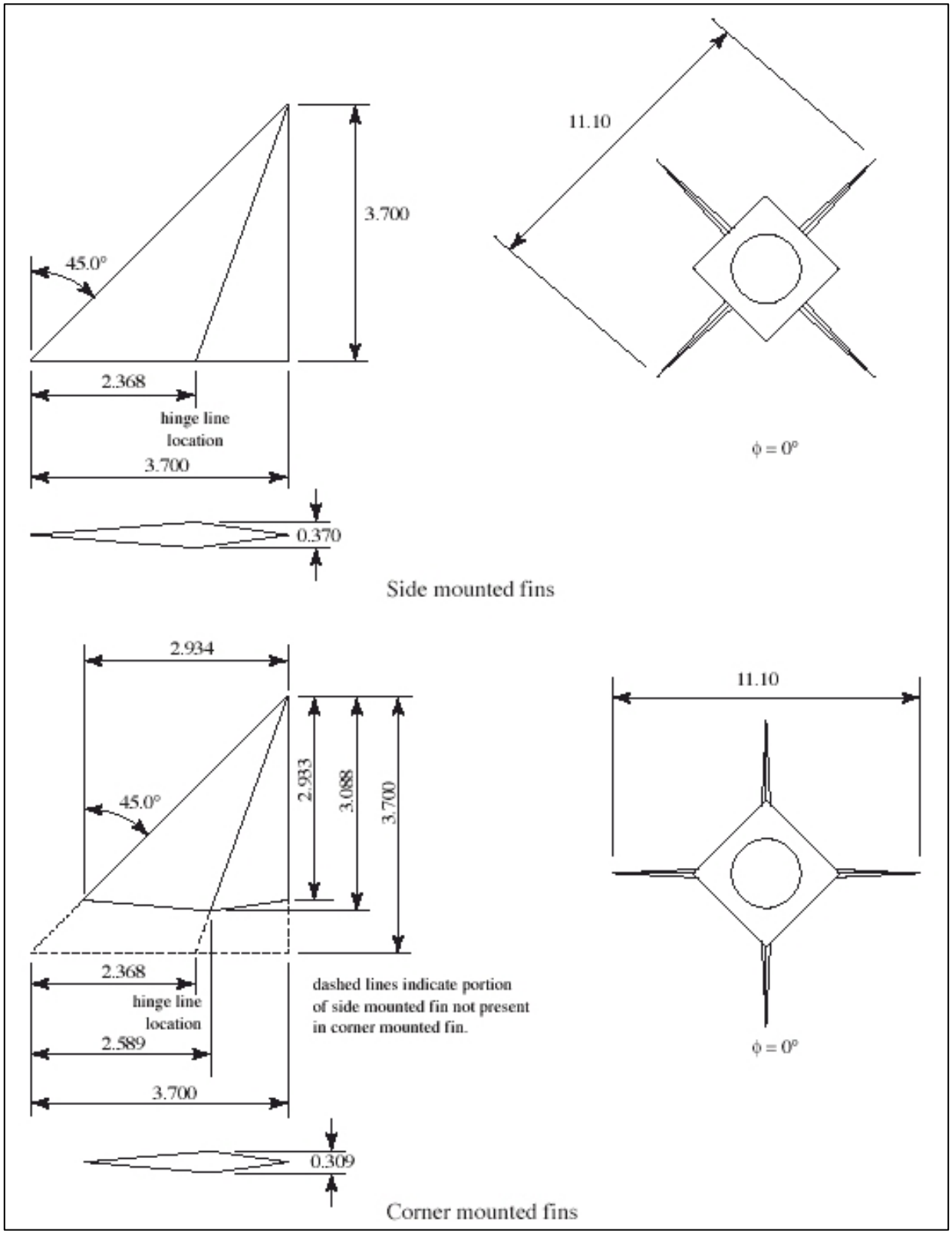

Figure 2. Sketch (inches) of side and corner mounted tail fins (*17*).

Figure 3. Corner fin configuration, side and base views.

Figure 4. Side fin configuration, side and base views.

4. Results and Discussion

Numerical computations using viscous Navier-Stokes methods were performed to predict the flow field and aerodynamic coefficients for wind tunnel test conditions. Thus, computations were conducted at Mach 2.5 and 4.5 for each configuration. Calculations were completed for each configuration at 0°, 22.5°, and 45° roll orientation, ϕ (figure 8). For each Mach number and roll orientation, calculations were completed at 14° angle of attack, α. For the side fin configuration at a roll orientation of 0° (figure 8d), a calculation was also performed for Mach 2.5 at 20° angle of attack. Full 3-D computations were performed and no symmetry was used.

4.1 Grid Resolution Study

A grid resolution study was conducted for the corner fin configuration at Mach 2.5, $\phi = 22.5°$, $\alpha = 14°$. The results of the $y^+ = 30$ grid, with the wall function option employed, were compared to that of the $y^+ = 1$ grid (table 1). Almost all coefficients were found to be within 1% or less. Only the rolling moment coefficient, C_l, had a greater discrepancy at 7%. This shows that either grid would be adequate for determining the aerodynamic coefficients. The $y^+ = 30$ grid was used for the Mach 2.5, $\phi = 0°$, $\alpha = 14°$ case. The $y^+ = 1$ grid was used for the remainder of the cases as the grid was smaller and required less computation time.

A grid resolution study was also conducted for the side fin configuration for the Mach = 2.5, $\phi = 0°$, $\alpha = 14°$ case (table 2). In this configuration, no side force, yawing moment, or rolling moment is expected. Again, almost all coefficients agreed to within 1%. For the coefficients expected to be near zero, small changes in value correspond to an unrealistically large percent error. Thus, percent difference is not calculated for these coefficients. The second grid did

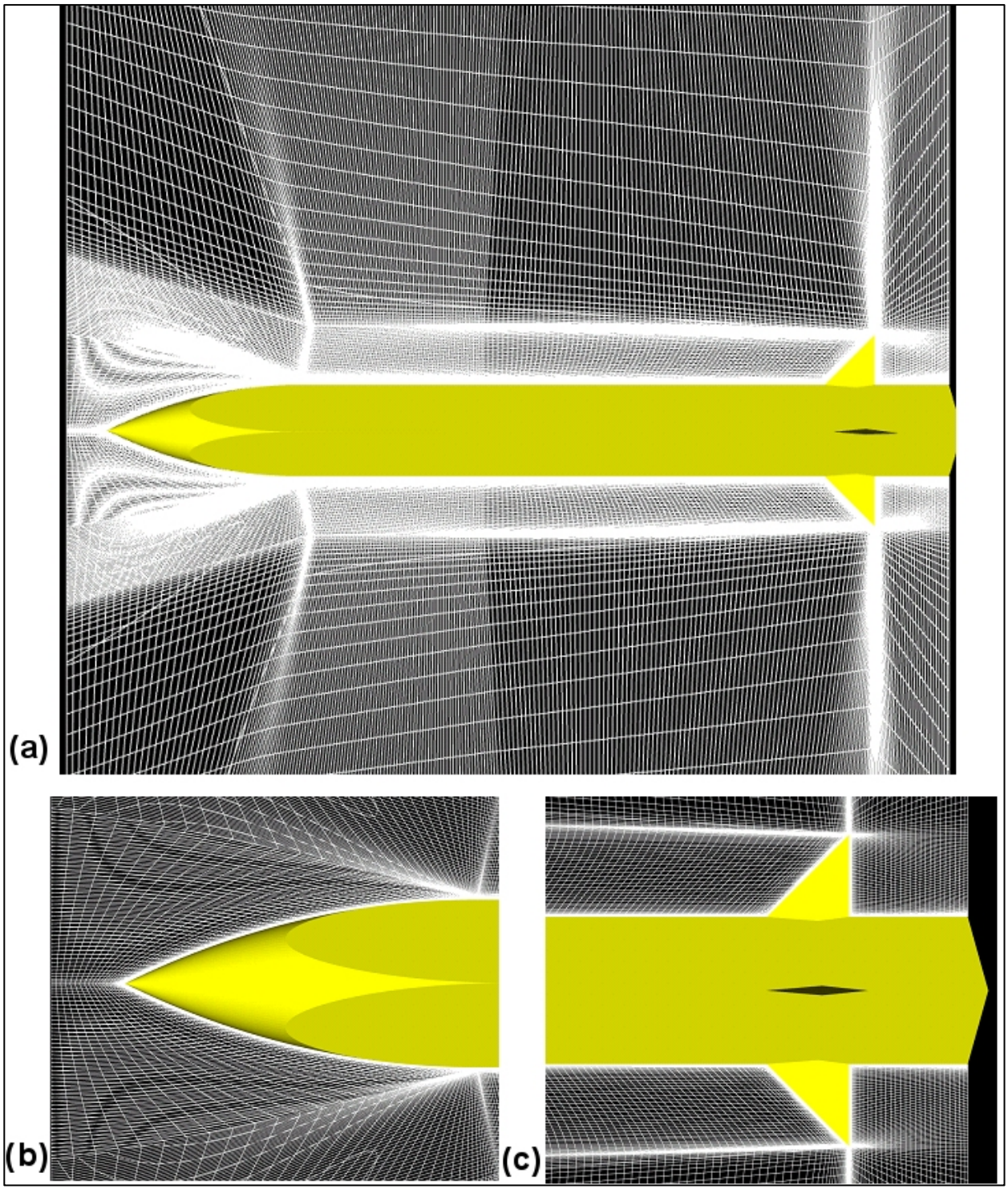

Figure 5. (a) Computational grid for corner fin geometry with $y^+ = 30$ spacing. Close-up of (b) nose tip and (c) fins.

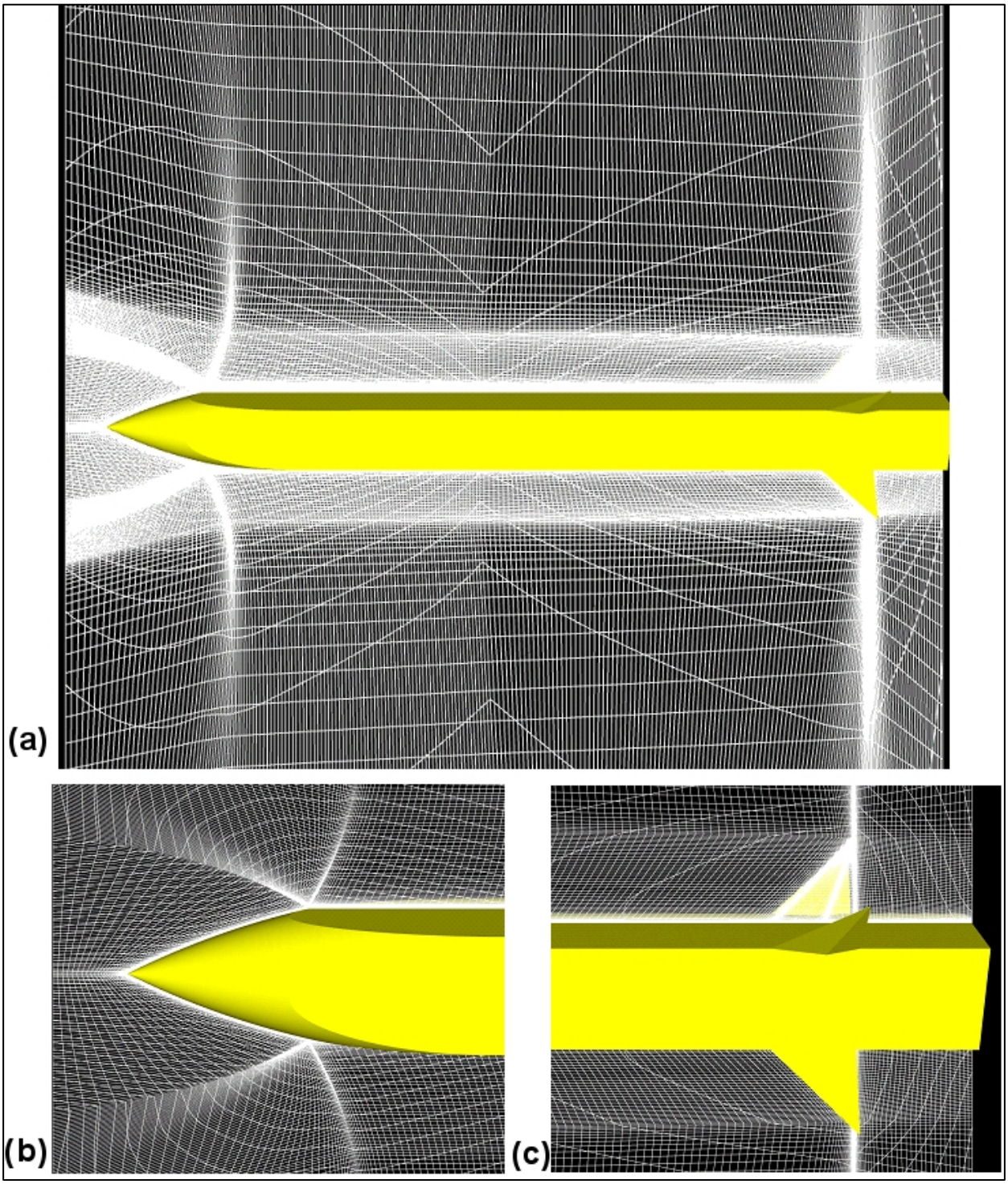

Figure 6. (a) Computational grid for corner fin geometry with $y^+ = 1$ spacing. Close-up of (b) nose tip and (c) fins.

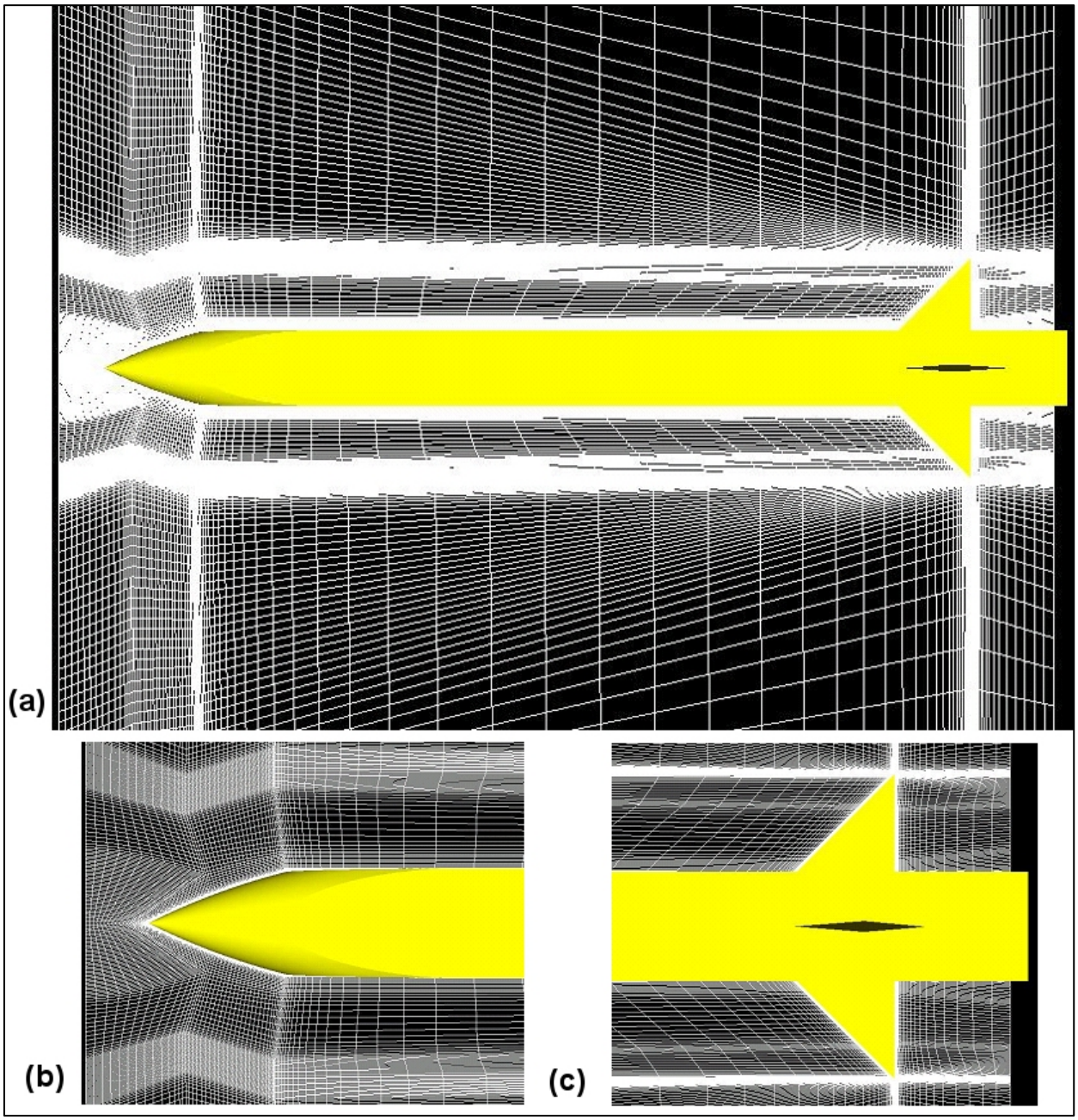

Figure 7. (a) Nine million hexahedral computational grid for side fin geometry with $y^+ = 1$ spacing. Close-up of (b) nose tip and (c) fins.

better in predicting the experimental normal force than the first grid. Also, CFD++ would not run for the first grid in some of the roll configurations. Therefore, the second grid (9.0 million hexahedral cells) was used for the remainder of the study.

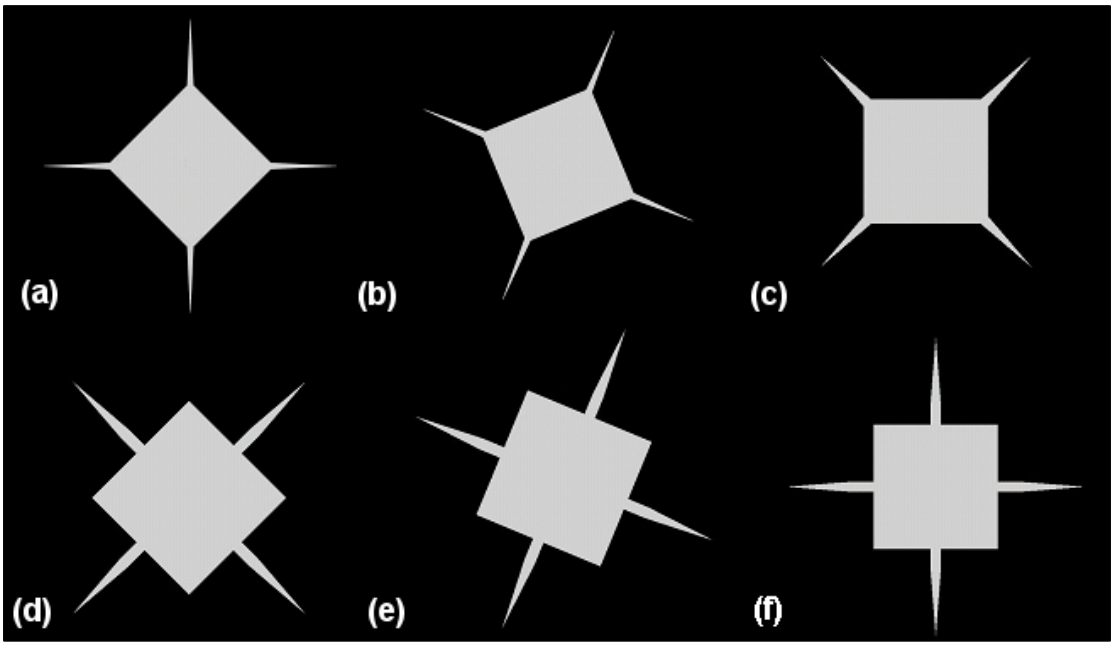

Figure 8. Roll orientation of 0°, 22.5°, and 45° for (a)–(c) corner fin projectile and (d)–(f) side fin projectile looking from projectile base.

Table 1. Grid resolution study for corner fin projectile at Mach 2.5, $\phi = 22.5°$, $\alpha = 14°$.

Coefficient	$y^+ = 30$	$y^+ = 1$	% difference
C_N	3.745	3.757	0.307
C_S	0.864	0.873	1.075
C_A	0.466	0.463	–0.683
C_L	3.521	3.533	0.338
C_D	1.358	1.358	–0.020
C_L/C_D	2.593	2.602	0.358
C_m	–24.685	–24.730	0.181
C_n	–7.598	–7.643	0.588
C_l	0.059	0.055	–7.054
X_{cp}	6.591	6.583	–0.127

Table 2. Grid resolution study for side fin projectile at Mach 2.5, $\phi = 0°$, $\alpha = 14°$.

Coefficient	Grid 1	Grid 2	% difference
C_N	4.017	4.014	0.065
C_S	0.000	0.000	—
C_A	0.492	0.488	0.814
C_L	3.778	3.777	0.041
C_D	1.449	1.444	0.312
C_L/C_D	2.608	2.615	–0.271
C_m	–26.014	–25.982	0.122
C_n	0.003	0.000	—
C_l	0.000	0.000	—
X_{cp}	6.477	6.473	0.057

4.2 Aerodynamic Coefficients

Aerodynamic coefficients including forces, moments, and center of pressure locations were determined for all cases. The moment reference is the nose-tip of the projectile. Comparing the computational results to the experimental results shows remarkably good agreement (tables 3–7). The values of axial force coefficient, C_A, normal force coefficient, C_N, and side force coefficient, C_S, are obtain directly from the experimental data and the numerical results. The values of lift coefficient, C_L, drag coefficient, C_D, and axial center of pressure, X_{CP}, are obtained from the following equations:

$$C_L = C_N \cos\alpha - C_A \sin\alpha \ , \tag{2}$$

$$C_D = C_N \sin\alpha + C_A \cos\alpha \ , \tag{3}$$

and

$$X_{CP} = -\frac{C_m}{C_N} \ , \tag{4}$$

where α is the flow angle of attack and C_m is the pitching moment.

As expected, C_A does not change significantly with fin location or roll orientation for either the experimental or the computational results (figure 9). C_A increases slightly for a given Mach number when comparing the corner fin configuration to side fin configuration, which is likely due to shock interaction effects due to fin location. For a given configuration, C_A decreases with increasing Mach number. The increase in angle of attack for the side fin configuration with a

Table 3. Aerodynamic coefficients for corner fin configuration at Mach 2.5, $\alpha = 14°$.

Coefficient	$\phi = 0°$		$\phi = 22.5°$		$\phi = 45°$	
	Exp	**CFD**	**Exp**	**CFD**	**Exp**	**CFD**
C_N	4.125	4.111	3.808	3.758	3.196	3.179
C_S	–0.0224	0.000	0.972	0.873	–0.049	0.001
C_A	0.480	0.467	0.475	0.463	0.476	0.466
C_L	3.886	3.876	3.580	3.534	2.986	2.972
C_D	1.464	1.448	1.382	1.358	1.235	1.221
C_L/C_D	2.654	2.677	2.590	2.602	2.418	2.434
C_m	–27.126	–27.289	–24.865	–24.738	–19.688	–19.809
C_n	0.167	0.002	–8.271	–7.645	0.375	–0.006
C_l	0.003	0.000	0.061	0.055	–0.004	0.000
X_{cp}	6.576	6.638	6.530	6.583	6.160	6.231

Table 4. Aerodynamic coefficients for corner fin configuration at Mach 4.5, $\alpha = 14°$.

Coefficient	$\phi = 0°$		$\phi = 22.5°$		$\phi = 45°$	
	Exp	**CFD**	**Exp**	**CFD**	**Exp**	**CFD**
C_N	3.108	3.082	2.949	2.904	2.778	2.743
C_S	0.011	0.000	0.260	0.219	–0.001	0.000
C_A	0.432	0.419	0.426	0.412	0.422	0.407
C_L	2.911	2.889	2.758	2.718	2.593	2.563
C_D	1.171	1.152	1.127	1.102	1.082	1.059
C_L/C_D	2.486	2.507	2.447	2.467	2.396	2.421
C_m	–20.315	–20.588	–18.924	–18.973	–17.263	–17.411
C_n	–0.124	0.002	–2.387	–2.029	–0.034	–0.001
C_l	0.000	0.000	0.062	0.066	0.001	0.000
X_{cp}	6.536	6.680	6.417	6.534	6.214	6.348

Table 5. Aerodynamic coefficients for side fin configuration at Mach 2.5, $\alpha = 14°$.

Coefficient	$\phi = 0°$		$\phi = 22.5°$		$\phi = 45°$	
	Exp	**CFD**	**Exp**	**CFD**	**Exp**	**CFD**
C_N	4.056	4.014	3.770	3.709	3.166	3.155
C_S	–0.020	0.000	0.885	0.814	–0.068	0.000
C_A	0.501	0.488	0.500	0.486	0.499	0.488
C_L	3.814	3.777	3.537	3.481	2.951	2.944
C_D	1.467	1.444	1.397	1.369	1.250	1.237
C_L/C_D	2.560	2.615	2.532	2.543	2.361	2.380
C_m	–26.134	–25.982	–24.286	–24.082	–19.286	–19.459
C_n	0.141	0.000	–7.287	–6.978	0.527	–0.001
C_l	–0.002	0.000	–0.053	–0.047	0.001	0.000
X_{cp}	6.443	6.473	6.442	6.494	6.092	6.167

Table 6. Aerodynamic coefficients for side fin configuration at Mach 4.5, $\alpha = 14°$.

Coefficient	$\phi = 0°$		$\phi = 22.5°$		$\phi = 45°$	
	Exp	**CFD**	**Exp**	**CFD**	**Exp**	**CFD**
C_N	3.110	3.087	2.950	2.906	2.773	2.735
C_S	0.004	0.000	0.255	0.204	–0.005	0.000
C_A	0.442	0.428	0.441	0.424	0.435	0.419
C_L	2.911	2.891	2.756	2.718	2.585	2.552
C_D	1.181	1.162	1.142	1.115	1.093	1.069
C_L/C_D	2.465	2.487	2.413	2.438	2.365	2.389
C_m	–20.301	–20.634	–18.873	–18.955	–17.137	–17.271
C_n	–0.064	–0.001	–2.343	–1.883	–0.007	0.000
C_l	0.000	0.000	0.0253	0.023	–0.003	0.000
X_{cp}	6.528	6.685	6.398	6.522	6.180	6.315

Table 7. Aerodynamic coefficients for side fin configuration at Mach 2.5, $\phi = 0°$, $\alpha = 20°$.

Coefficient	Exp	CFD
C_N	6.784	6.714
C_S	–0.017	0.000
C_A	0.526	0.510
C_L	6.195	6.135
C_D	2.815	2.776
C_L/C_D	2.201	2.210
C_m	–45.751	–45.543
C_n	0.138	–0.001
C_l	0.000	0.000
X_{cp}	6.744	6.783

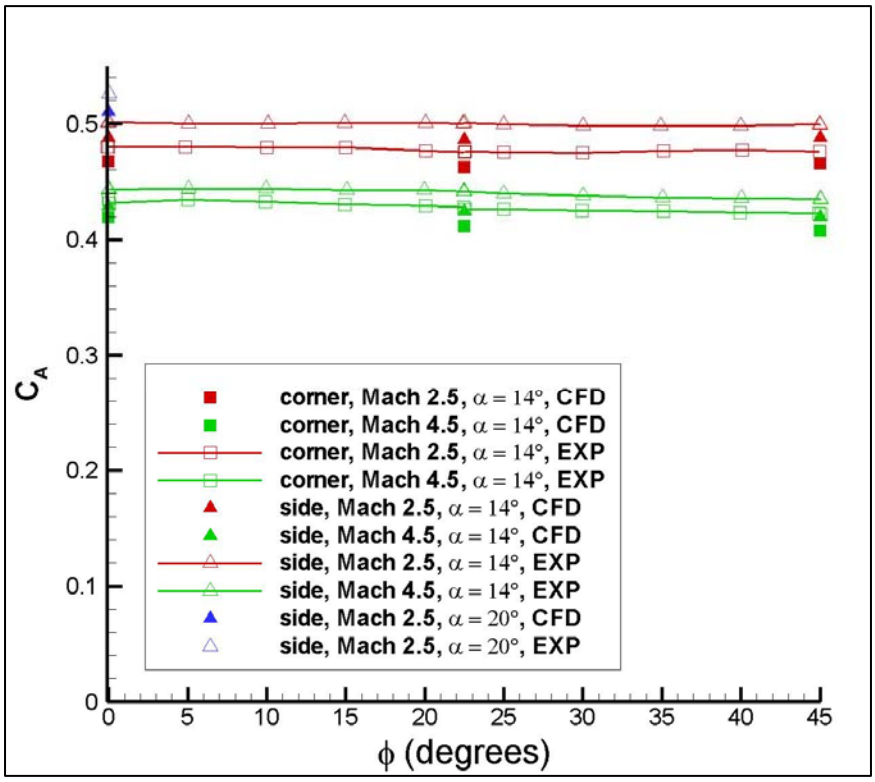

Figure 9. Axial force coefficient as a function of roll orientation.

constant Mach number of 2.5 caused an increase in C_A. For the roll angles investigated computationally, regardless of Mach number or angle of attack, there is a small, but consistent, under prediction of the experimental C_A. Perhaps the boundary layer is not completely resolved or a different turbulence model should have been used.

The computed C_N agrees very well with the experimental data (figure 10). The maximum normal force occurs for $\phi = 0°$, regardless of the fin configuration and decreases as the body is rolled. Fin location has a negligible effect on C_N, as C_N for a given Mach number and angle of

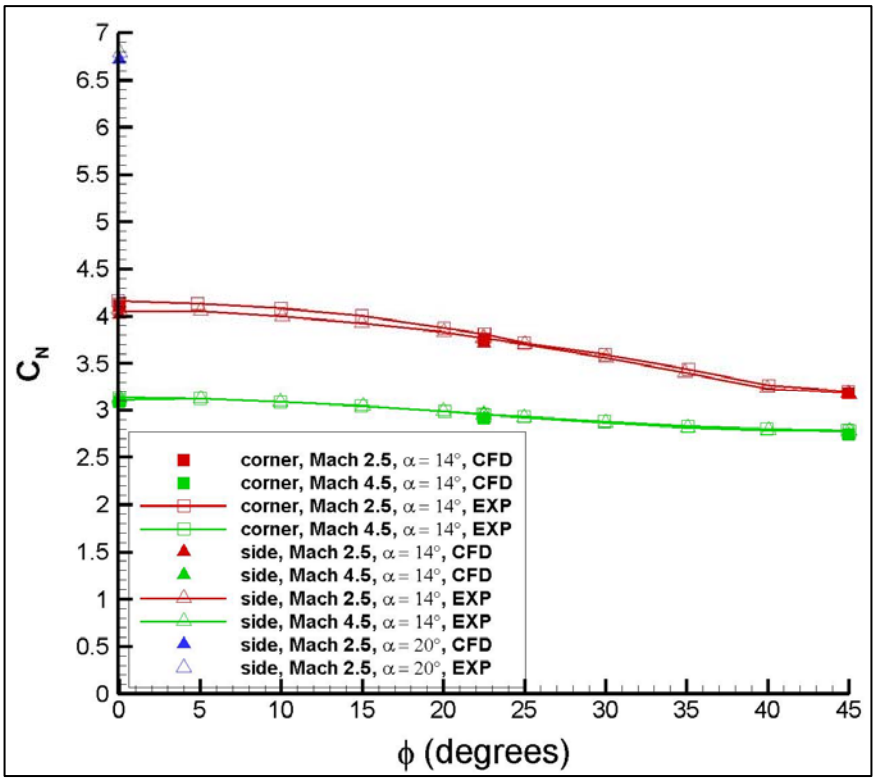

Figure 10. Normal force coefficient as a function of roll orientation.

attack is nearly identical regardless of the fin location. This implies that body orientation has a greater influence on C_N that does fin configuration. The increase in C_N with angle of attack was expected.

At Mach 4.5, C_S does not vary significantly with fin location (figure 11). At Mach 2.5, C_S increases a greater amount (to a 10% maximum) for the corner fin projectile than the side fin projectile as it rolls from the $\phi = 0°$ orientation to the $\phi = 22.5°$ position. The difference then decreases as the roll progresses from $\phi = 22.5°$ to $\phi = 45°$, suggesting that the flow is affected by the asymmetries. The computational results show the same trends as the experimental data. CFD accurately predicts the lack of side force at $\phi = 0°$ and $\phi = 45°$. However, there seems to be an offset from the experimental data at $\phi = 22.5°$. Perhaps the shock interactions are not fully resolved.

The rolling moment coefficient, C_l, shows good agreement between the CFD and experimental data at Mach 4.5 (figure 12). At Mach 2.5, however, there seems to be a small discrepancy $\phi = 22.5°$. The Mach 2.5, $\alpha = 14°$ side fin configuration shows roll in the opposite direction from the rest of the cases investigated. This is likely due to large differences in vortex development for this case. The remainder of the data is as expected, with larger rolling moment coefficients existing for higher Mach numbers, angles of attack, and deviation from a symmetric roll orientation.

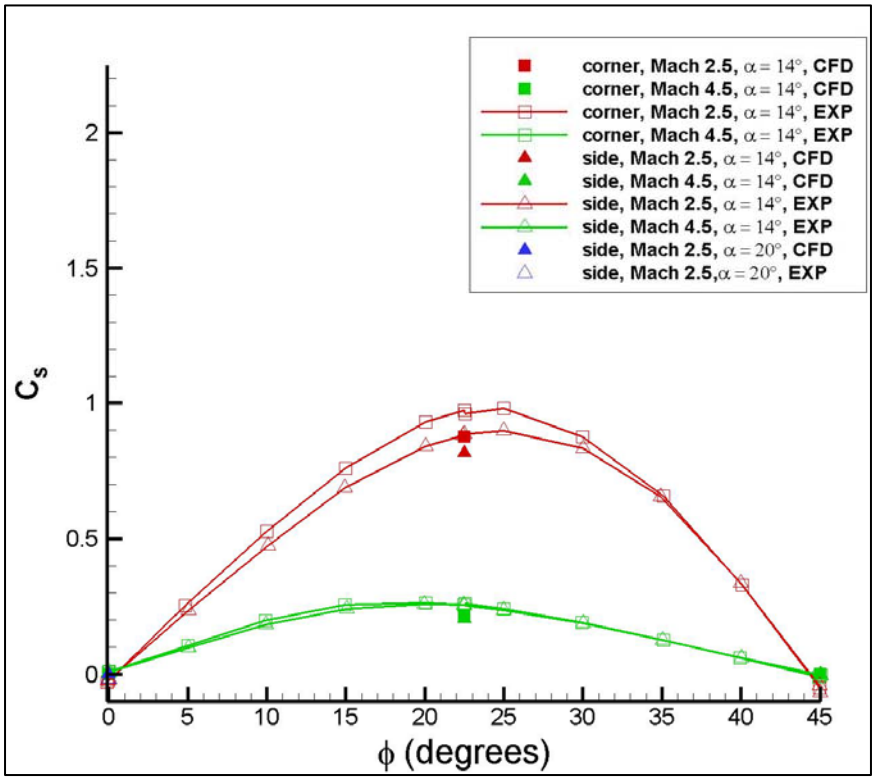

Figure 11. Side force coefficient as a function of roll orientation.

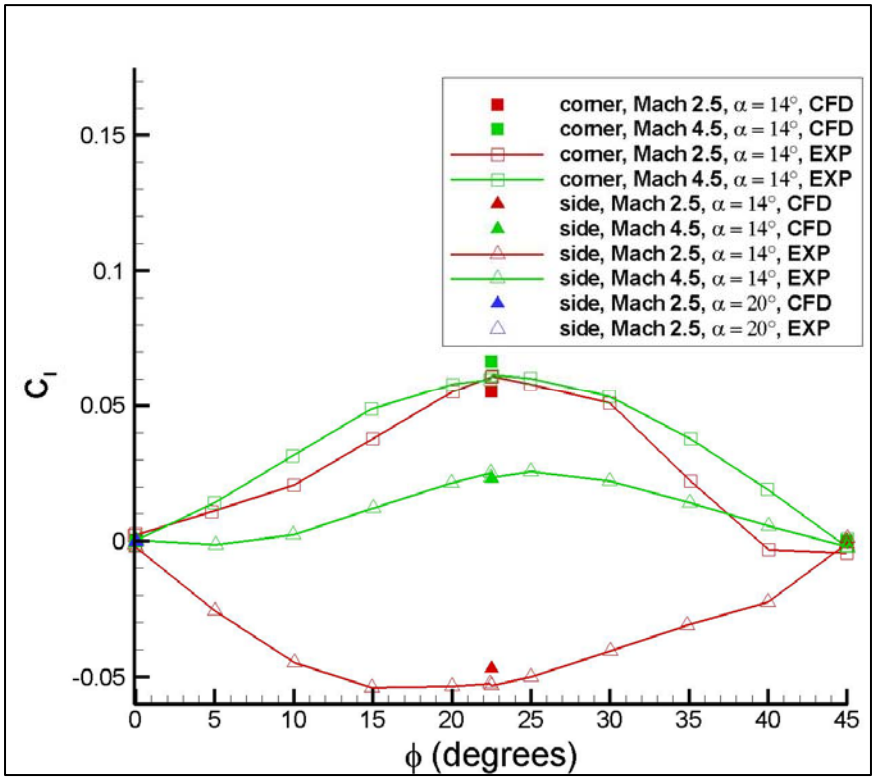

Figure 12. Rolling moment coefficient as a function of roll orientation.

The pitching moment coefficient, C_m, also shows good agreement between the CFD and experimental data (figure 13). The trend of these coefficients appears to be a mirror image of the normal force coefficient trend, which would be expected, and there is little variation with fin location. It is interesting that the largest magnitude pitching moment coefficients occur at $\phi = 0°$

However, it is not unexpected that the largest variation with roll orientation occurs for the largest angle of attack. Unfortunately, the experimental data was provided with a moment reference point of the nose. This does not allow for a good determination of the dominating flow characteristics (most likely the tail) or the true sensitivity of the pitching moment coefficient.

The yawing moment coefficient, C_n (figure 14), show trends similar to those of the side force coefficient. The largest magnitude coefficient occurs at $\phi = 22.5°$ and decreases as the symmetric roll orientations are approached. There is a larger difference in the coefficient at the same roll orientation between the two fin locations for Mach 2.5 than Mach 4.5. There is less yawing moment at Mach 4.5 than Mach 2.5 for a given angle of attack. Although not very noticeable in figure 14, tables 3–7 show that the CFD is underpredicting the yawing moment coefficient by as much as 0.5. This is as likely due to experimental error (there appears to be an offset in C_n as its value is not exactly zero when one expects it to be) as due to discrepancies in the computations.

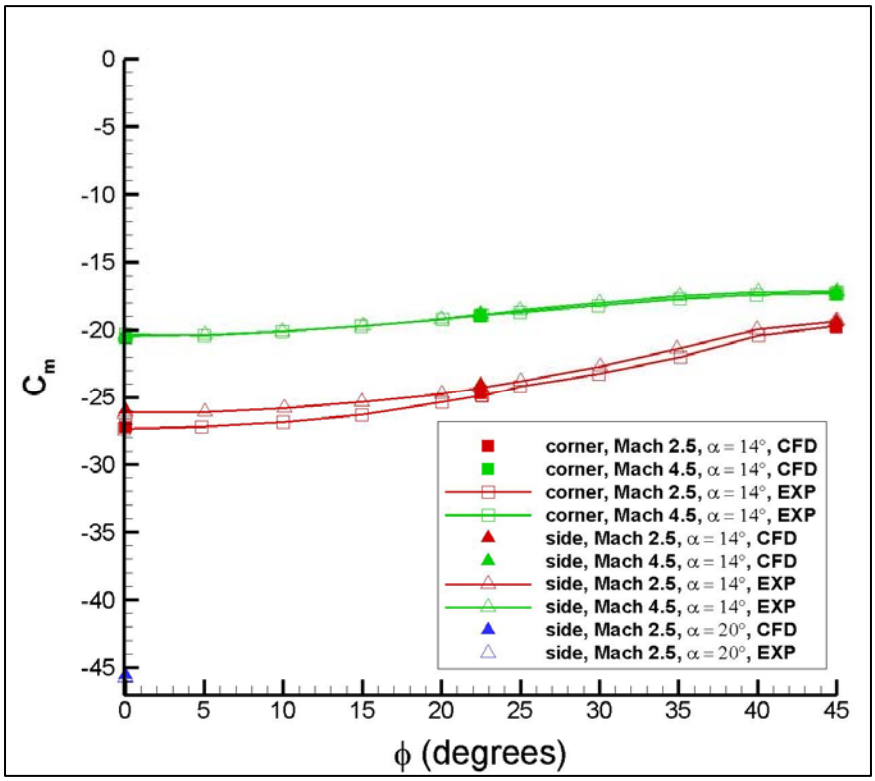

Figure 13. Pitching moment coefficient as a function of roll orientation.

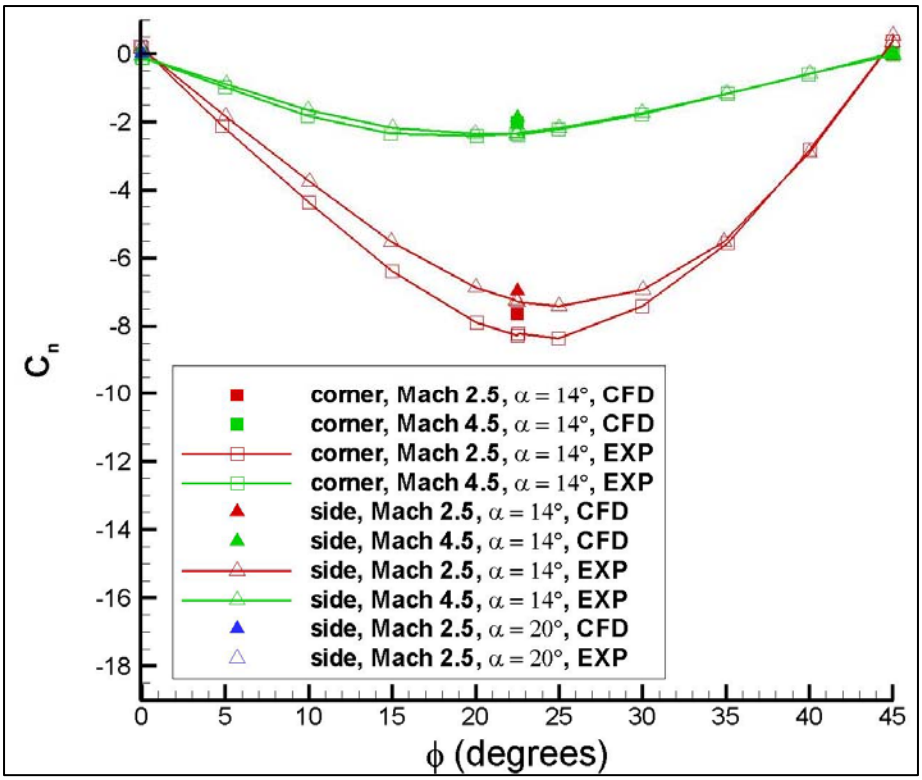

Figure 14. Yawing moment coefficient as a function of roll orientation.

4.3 Pressure Coefficient Distributions

Surface pressure coefficient, C_p, distributions were obtained for each simulation at four axial body positions with respect to the reference diameter of the body, D; x/D = 5.5, 8.5, 11.5, and 12.5. These locations correspond to one-third and two-thirds of the way down stream on the body, the midpoint of the root chord of the fin and aft of the fin, respectively (figure 15). The numerical results were compared to the results of the wind tunnel tests for each $\alpha = 14°$ simulation at the x/D = 5.5 and 8.5 locations with fair success. For each configuration, two experimental data sets were available. As a measure of experimental error, both data sets are plotted (labeled exp1 and exp2 in all C_p figures).

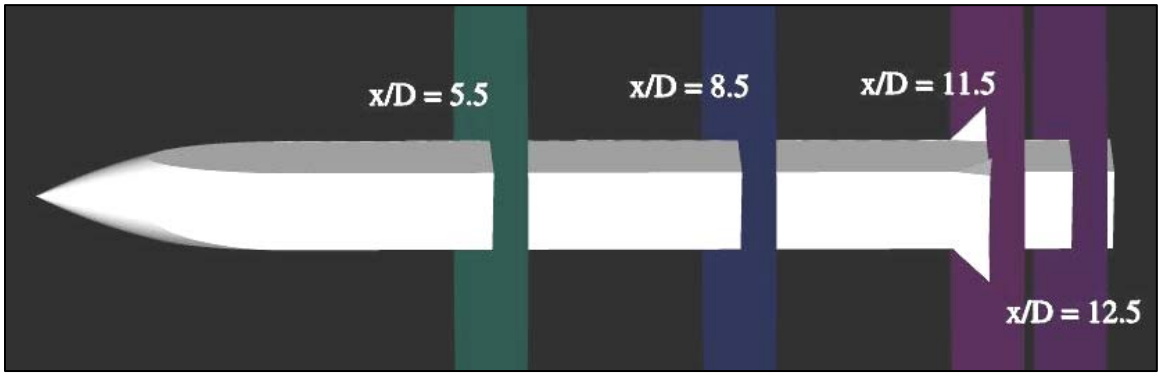

Figure 15. Reference axial body position locations on corner fin configuration.

Figures 16–18 show these results for the x/D = 5.5 location. As expected, the pressure distributions of the side and corner fin geometries are the same for each configuration at these x/D locations as they are located upstream up stream of the fins. At $\phi = 0°$ (figure 16), the pressure distribution is quite accurately predicted on the leeward side regardless of Mach number. On the windward side of the projectile, the trends are fairly well predicted, but the magnitude is slightly high. For the $\phi = 22.5°$ (figure 17) and $\phi = 45°$ (figure 18) roll orientations, the pressure distributions are more accurately predicted at Mach 4.5 than at Mach 2.5. This is likely because the gradients are steeper for Mach 2.5. The trends for the x/D = 8.5 location are nearly the same at for x/D = 5.5. Figures 19–21 show the results for the x/D = 8.5 location.

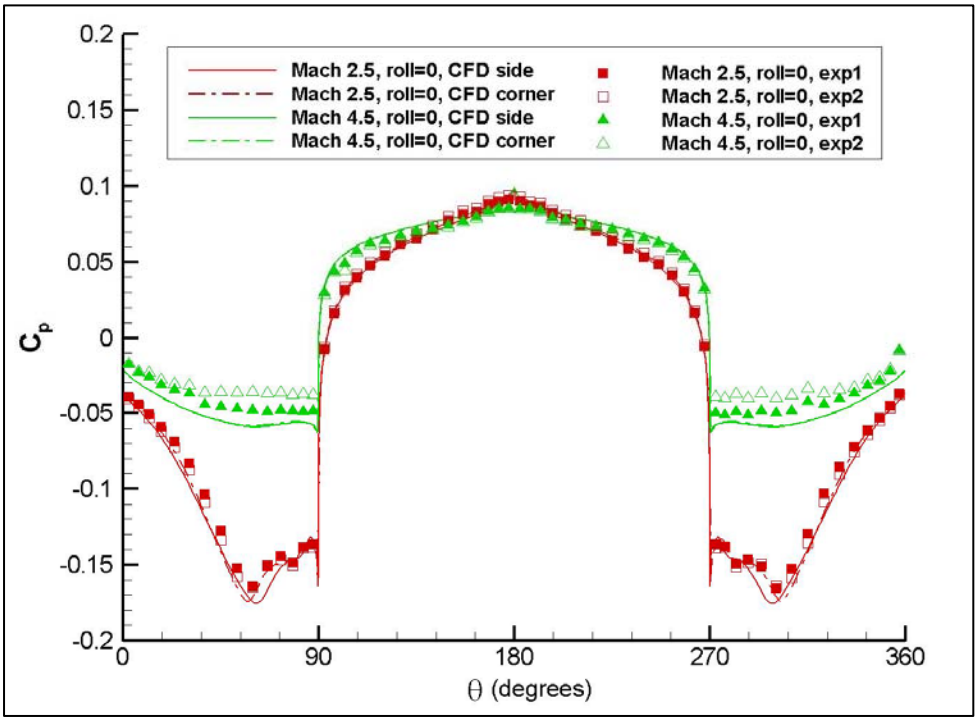

Figure 16. Pressure coefficient distribution at x/D = 5.5, $\phi = 0°$, $\alpha = 14°$.

For x/D = 11.5 and x/D = 12.5, no wind tunnel data was provided for the projectile with fins at $\alpha = 14°$ in any roll orientation. The numerical results for each roll orientation at x/D = 11.5 are shown in figure 22. At this location, C_p was obtained only on the body surface and not on the fins. As such, data is plotted with symbols and the discontinuity in the data is the location of the fins. For the $\phi = 0°$ roll orientation (figure 22a), the surface pressures are consistently greater at Mach 2.5 than at Mach 4.5 for the side fin configuration, while the inverse in true for the corner fin configuration. Additionally, the pressure coefficient for the side fin configuration is consistently greater than the corner fin configuration regardless of Mach number except in the vicinity of the fin. As the roll orientation is changed to $\phi = 22.5°$ (figure 22b), the flow becomes very complicated as it is completely asymmetric. This complexity carries over to the surface

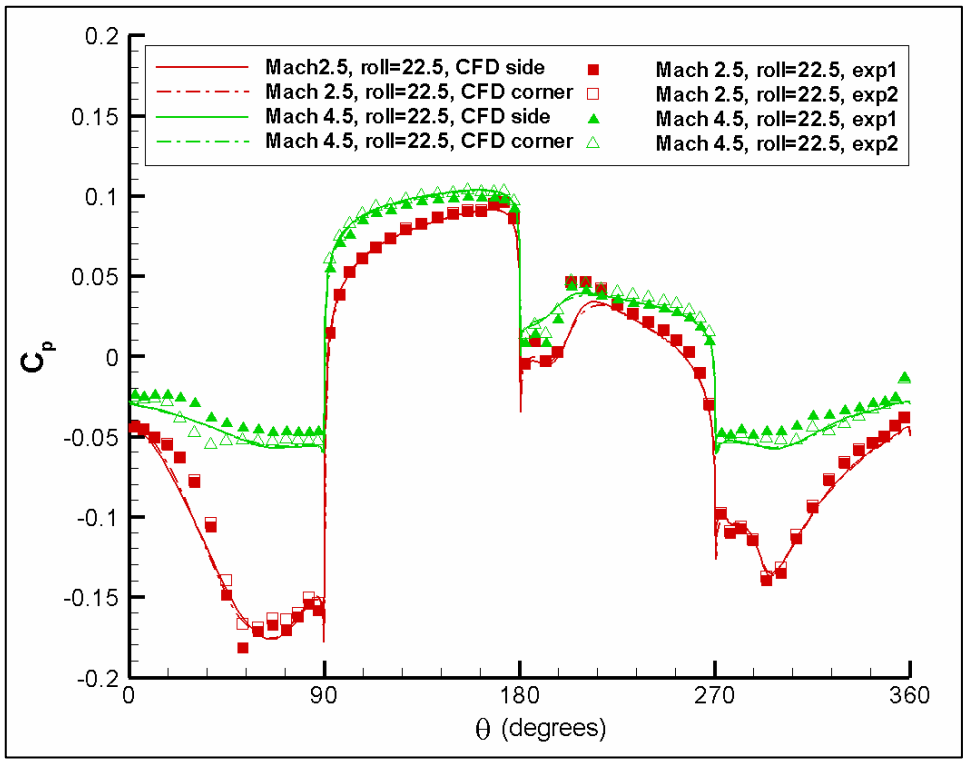

Figure 17. Pressure coefficient distribution at x/D = 5.5, $\phi = 22.5°$, $\alpha = 14°$.

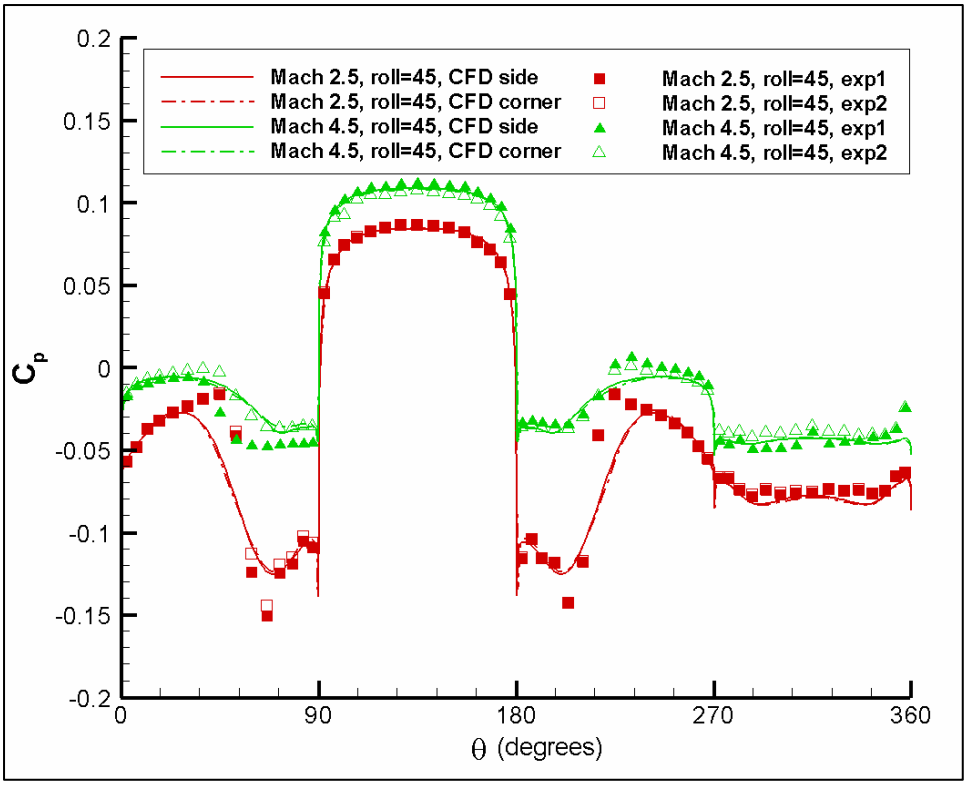

Figure 18. Pressure coefficient distribution at x/D = 5.5, $\phi = 45°$, $\alpha = 14°$.

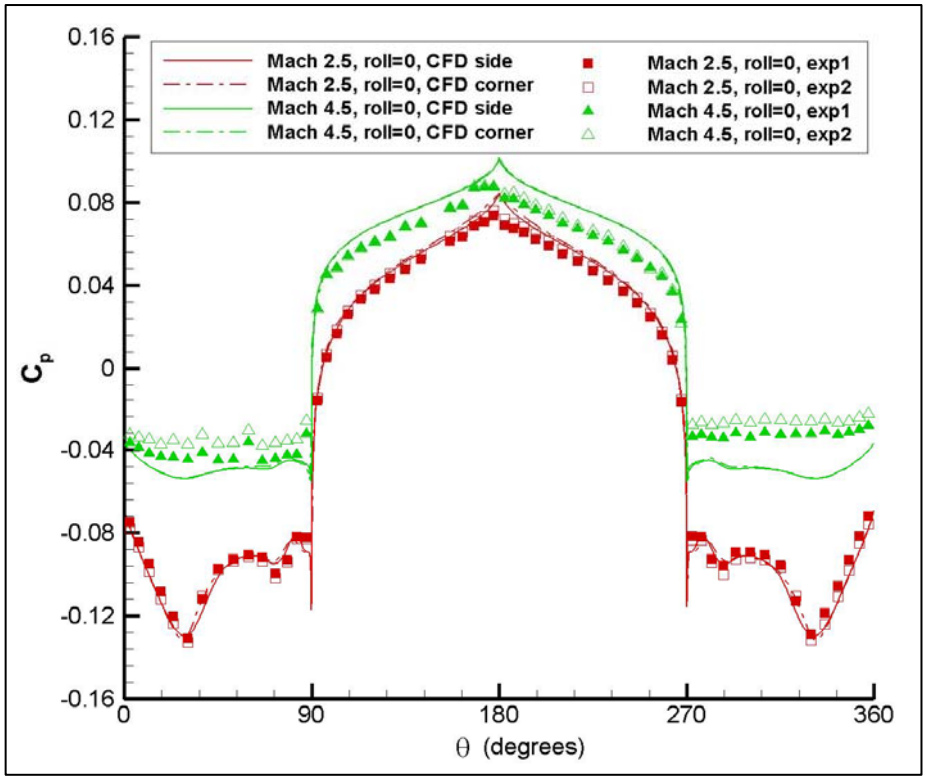

Figure 19. Pressure coefficient distribution at x/D = 8.5, $\phi = 0°$, $\alpha = 14°$.

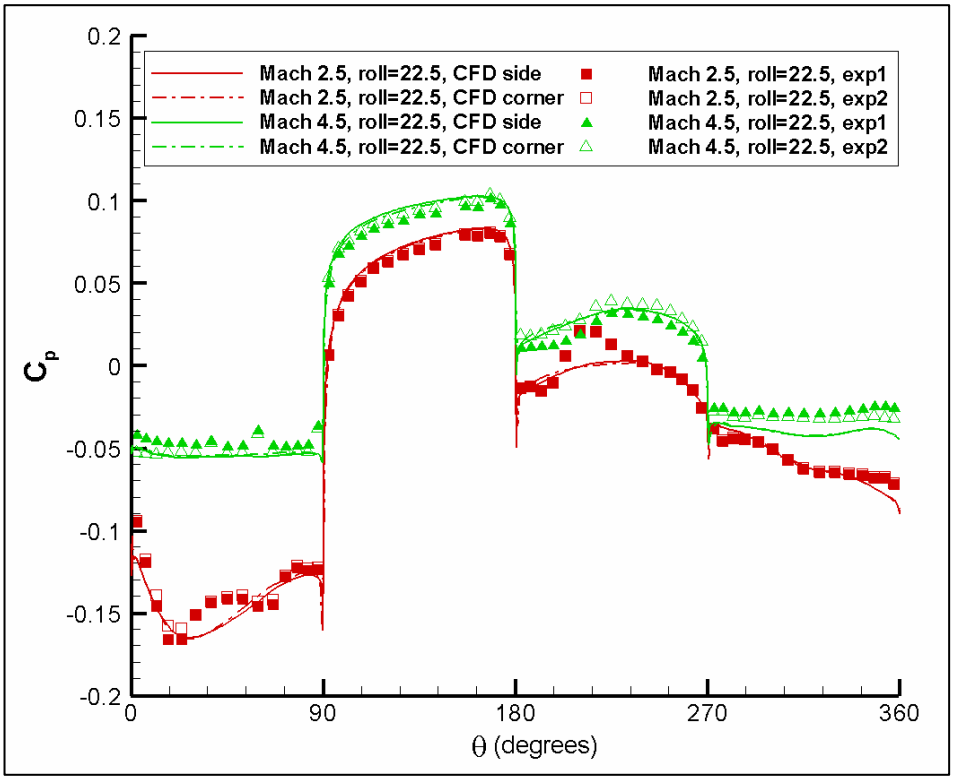

Figure 20. Pressure coefficient distribution at x/D = 8.5, $\phi = 22.5°$, $\alpha = 14°$.

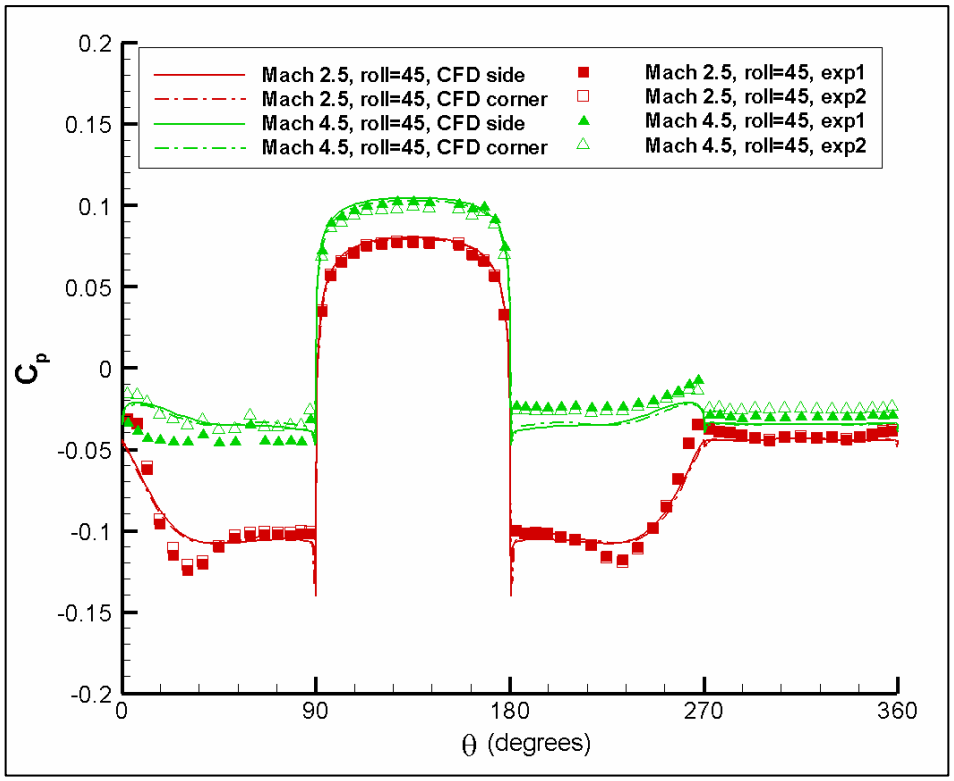

Figure 21. Pressure coefficient distribution at x/D = 8.5, $\phi = 45°$, $\alpha = 14°$.

pressure distributions as can be seen in figure 22b. The one noticeable difference at this roll orientation is that the surface pressure coefficients at Mach 4.5 are almost always greater than those at Mach 2.5 for given configuration. At $\phi = 45°$, the flow becomes more symmetrical. In terms of surface pressure distribution (figure 22c), symmetry exists about $\theta = 145°$ if one looks at $0° < \theta < 270°$.

As one moves downstream of the fins to x/D = 12.5, the surface pressure coefficient distributions once again become easier to interpret, though the influence of the fins is still present as would be expected (figure 23). Areas of increased surface pressure remain at the surface locations where the fin were located. This causes "bulges" in the curves.

Experimental C_p distributions were not available for the Mach 2.5, $\phi = 0°$, $\alpha = 20°$ side fin configuration either. The numerical results are compared to the Mach 2.5, $\phi = 0°$, $\alpha = 14°$ side fin configuration at each x/D location in figure 24. While the surface pressure distributions remain symmetric due to body orientation, there is a significant change in C_p along the entire length of the body as the angle of attack is increased from 14° to 20° for the same flow conditions and model orientation. Over the top side of the body ($0° \leq \theta < 90°$ and $270° \leq \theta < 360°$), the pressure coefficient is more negative for the higher angle of attack, while on the bottom side of the body ($90° \leq \theta \leq 270°$), the pressure coefficient is more positive. This confirms the increase in lift that is generated at the higher angle of attack.

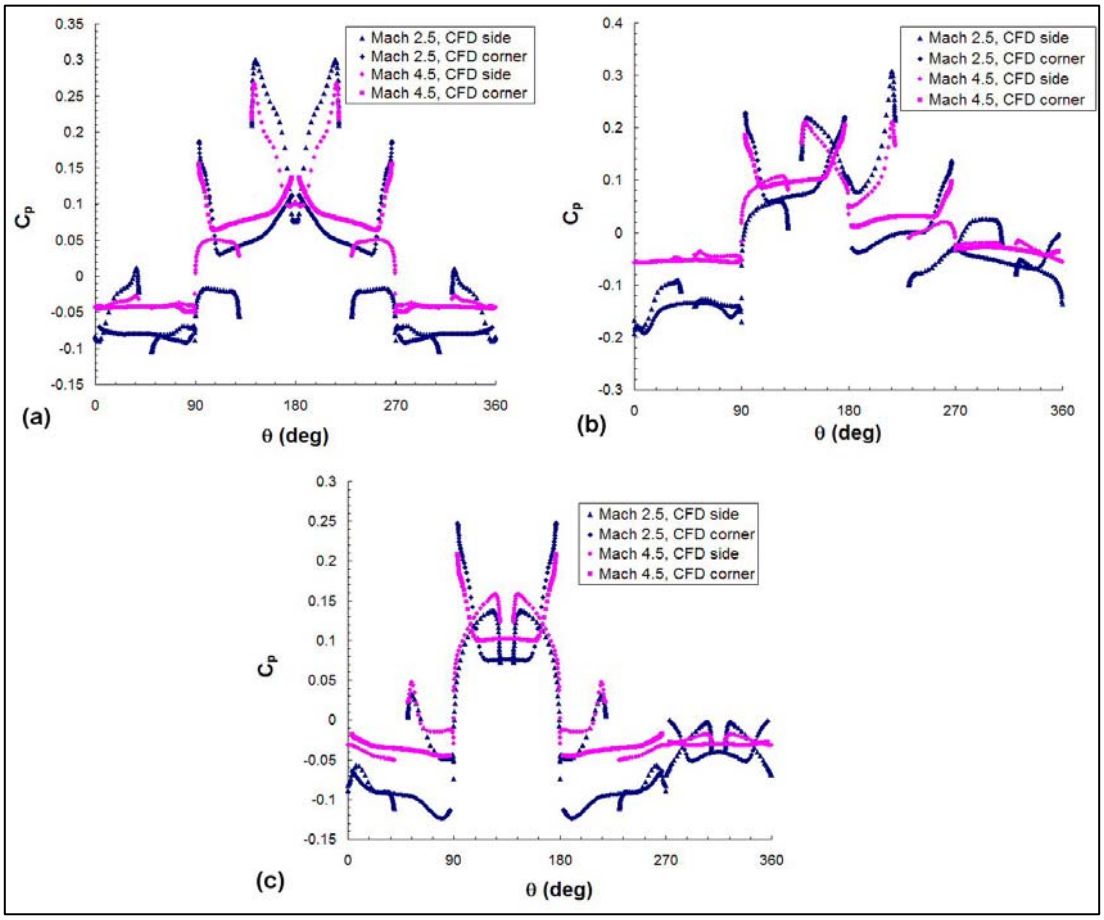

Figure 22. Pressure coefficient distribution at x/D = 11.5. (a) $\phi = 0°$, $\alpha = 14°$, (b) $\phi = 22.5°$, $\alpha = 4°$, (c) $\phi = 45°$, $\alpha = 14°$.

4.4 Flowfield Visualizations

Flow field visualizations were completed for each configuration, orientation, and flow conditions at the same four axial body position locations for which the pressure coefficient distributions were obtained (i.e., x/D = 5.5, 8.5, 11.5, and 12.5). Figures 25–30 show 3-D plots of pitot pressure and vorticity for both fin configurations at all three roll angles for the Mach 2.5 flow. The vortex cores are seen in both the pitot pressure contours as well as the vorticity contours. The contours are symmetric, as expected for $\phi = 0°$ and $\phi = 45°$ and asymmetric for $\phi = 22.5°$, regardless of fin location. For all configurations, the vortex cores grow and move away from the body as they move downstream.

Figure 31 shows the results of the Mach 2.5 flow at 20° angle of attack. The vortex cores are much larger and more elongated than the 14° angle-of-attack case. The vortex cores also appear to become more disorganized and weaker as they pass over the fins than at the lower angle of attack.

Figures 32–37 show the results of the Mach 4.5 flow. The overall flow structure remains practically the same as for the Mach 2.5 flow. The biggest difference that one notices is that the

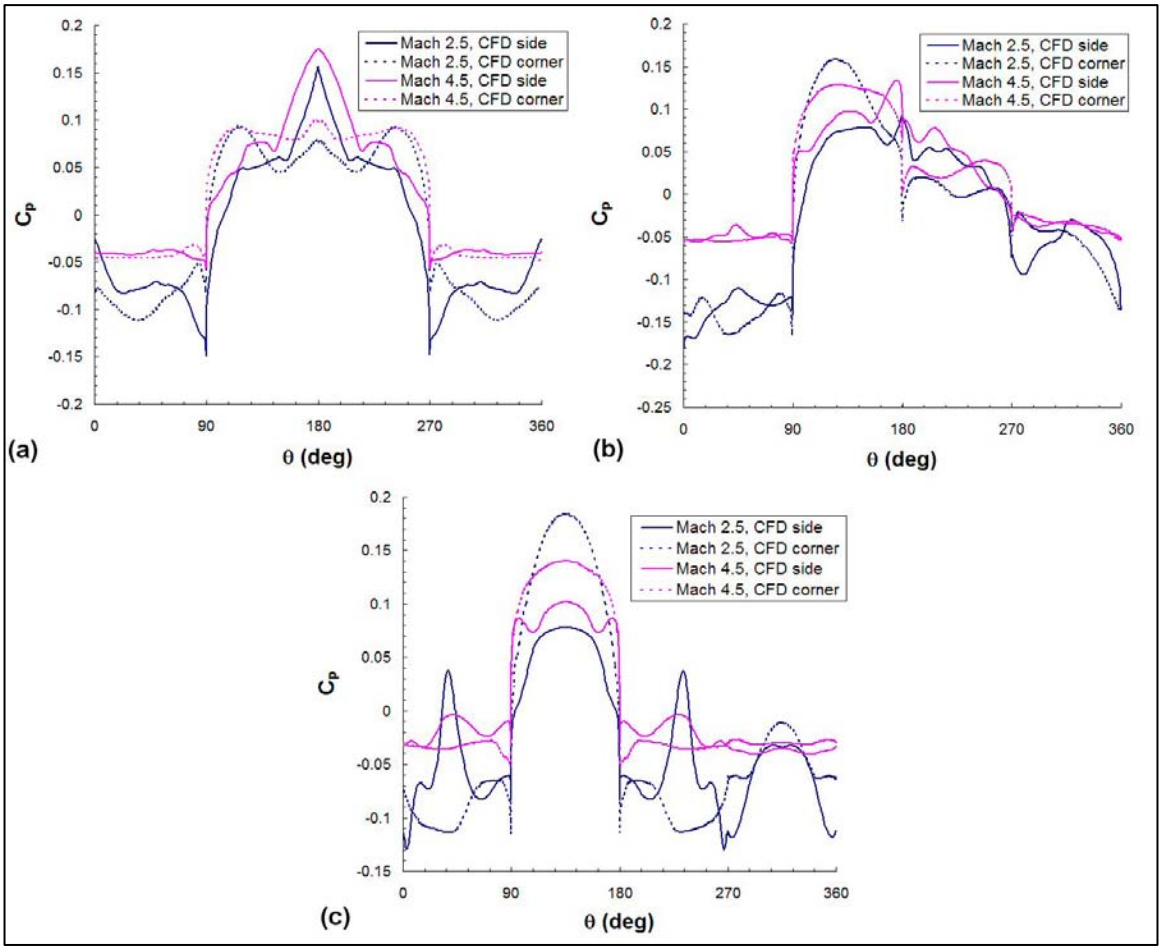

Figure 23. Pressure coefficient distribution at x/D = 12.5. (a) $\phi = 0°$, $\alpha = 14°$, (b) $\phi = 22.5°$, $\alpha = 14°$, (c) $\phi = 45°$, $\alpha = 14°$.

vortex cores are no longer circular upstream of the fins (x/D = 5.5 and 8.5) as they were at Mach 2.5, $\alpha = 14°$. As these figures again show that the flow structure can easily be seen in either the pitot pressure contours or the vorticity contours, either vorticity contours or pressure contours are presented for the remainder of this section.

The visualizations for x/D = 5.5 and 8.5 (upstream of the fins) do not vary with fin location (figures 38 and 39, respectively) as the flow is supersonic and therefore the downstream geometric differences do not effect the upstream flow. However, the flow structure does vary with roll (figures 38 and 39), angle of attack (figure 40), and Mach number (figure 41) as would be expected. The visualizations at the two further aft positions are much more interesting due to the influence of the geometric influences.

If one first compares the effect of fin location on pressure and vorticity contours at x/D = 11.5, it is easy to see that the areas of high pressure are limited to a very small region near the fins, regardless of roll orientation (figure 42), while the areas of low pressure, large circulation, and vorticity depend more on roll orientation than fin location (figure 43). The pitch-plane symmetry of the flow at $\phi = 0°$ and $\phi = 45°$ is quite noticeable as is the complete asymmetry at $\phi = 22.5°$ regardless of fin position.

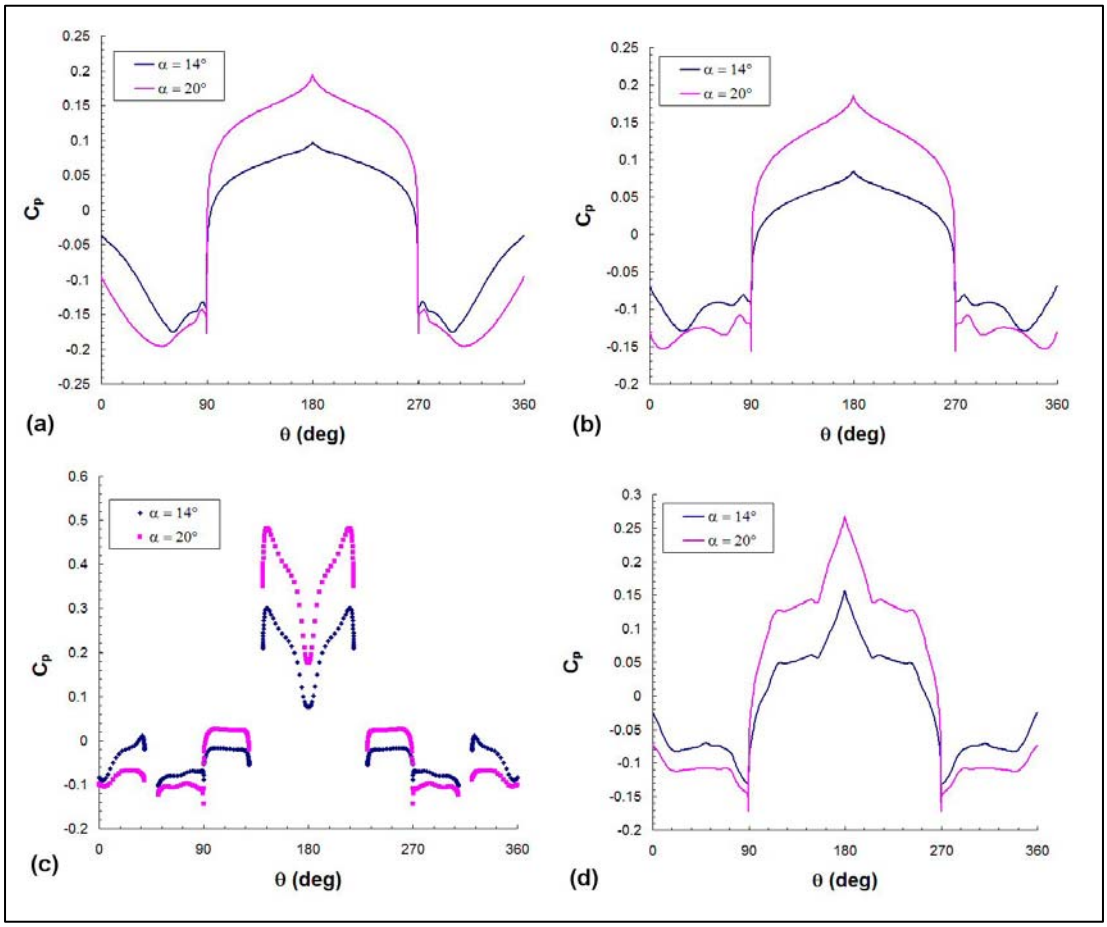

Figure 24. Pressure coefficient distribution for Mach 2.5 and $\phi = 0°$ at (a) x/D = 5.5, (b) x/D = 8.5, (c) x/D = 11.5, and (d) x/D = 12.5.

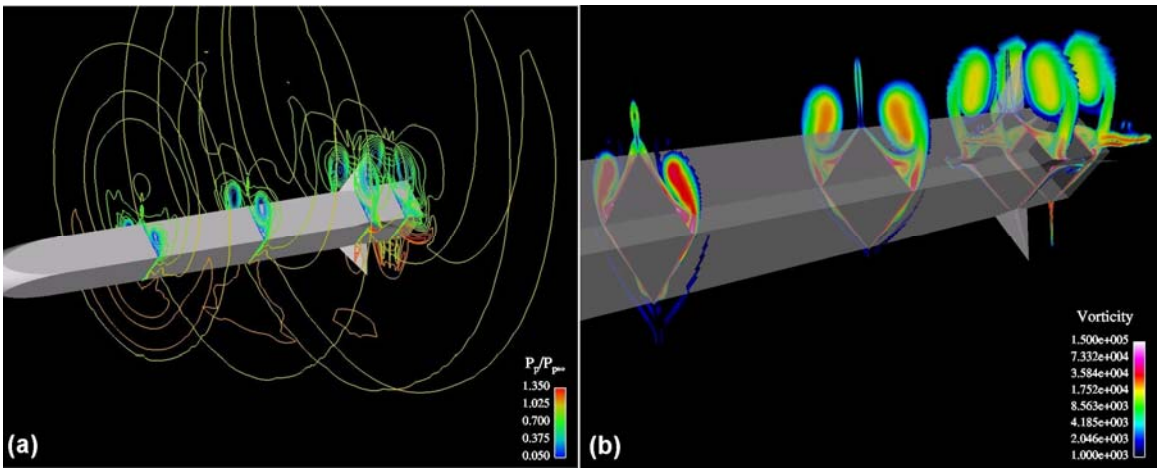

Figure 25. Three-dimensional (a) pitot pressure contours and (b) vorticity contours for corner fin configuration, Mach 2.5, $\phi = 0°$, $\alpha = 14°$.

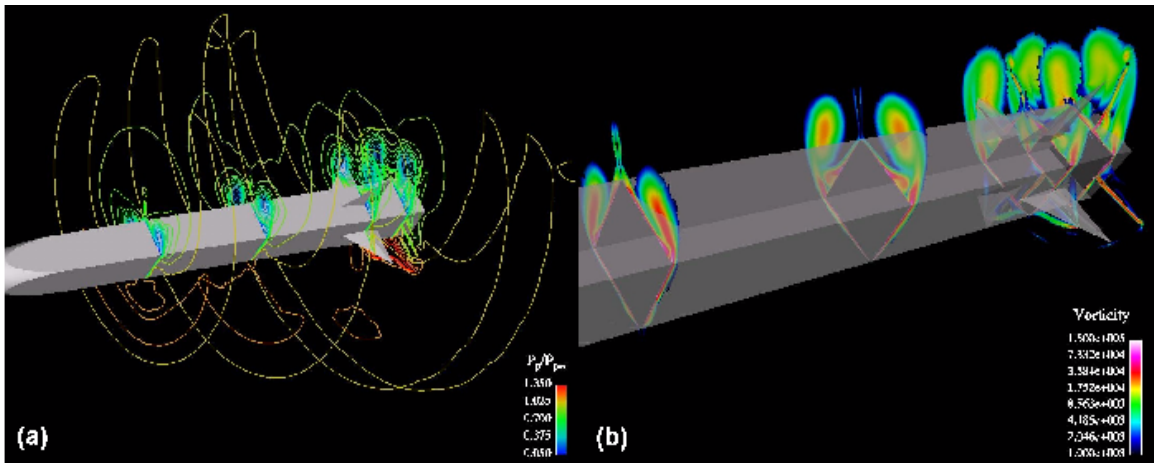

Figure 26. Three-dimensional (a) pitot pressure contours and (b) vorticity contours for side fin configuration, Mach 2.5, $\phi = 0°$, $\alpha = 14°$.

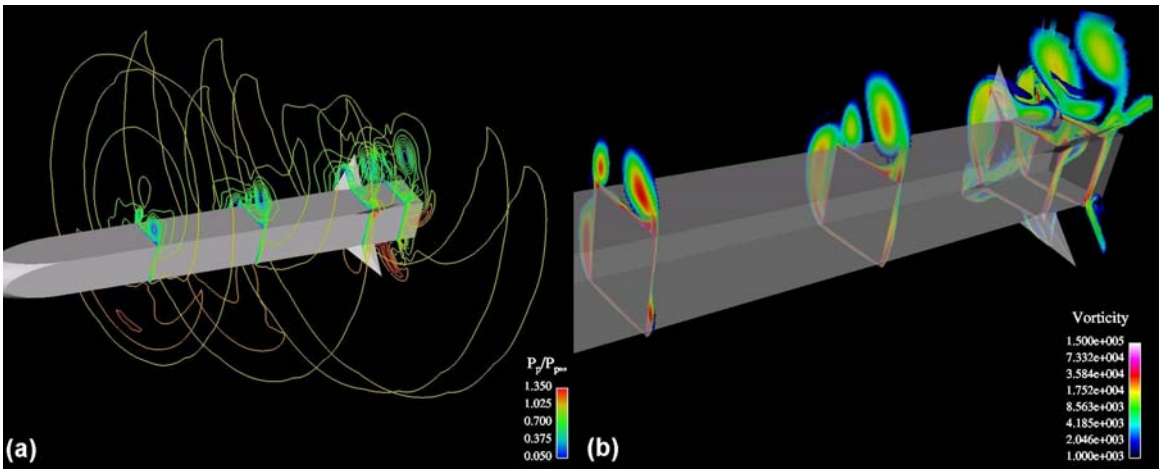

Figure 27. Three-dimensional (a) pitot pressure contours and (b) vorticity contours for corner fin configuration, Mach 2.5, $\phi = 22.5°$, $\alpha = 14°$.

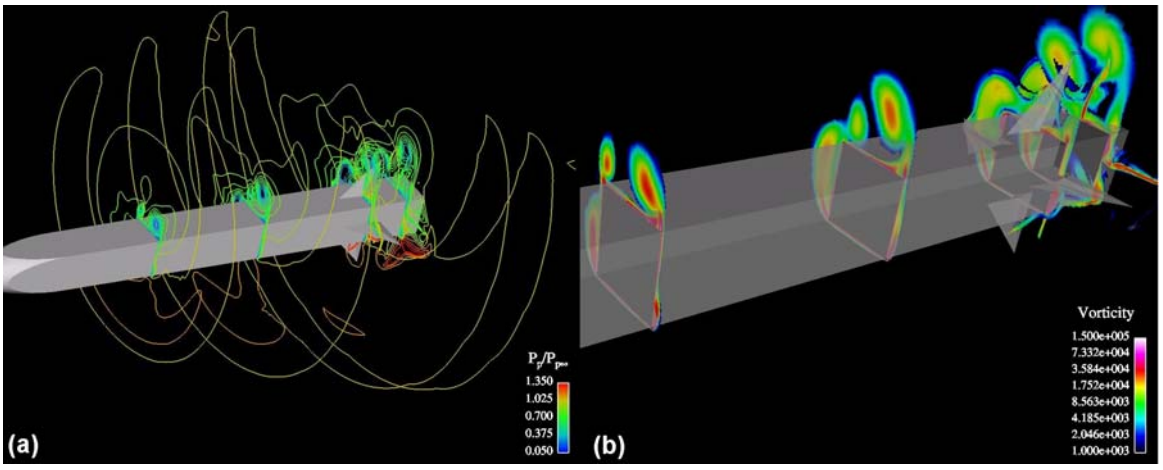

Figure 28. Three-dimensional (a) pitot pressure contours and (b) vorticity contours for side fin configuration, Mach 2.5, $\phi = 22.5°$, $\alpha = 14°$.

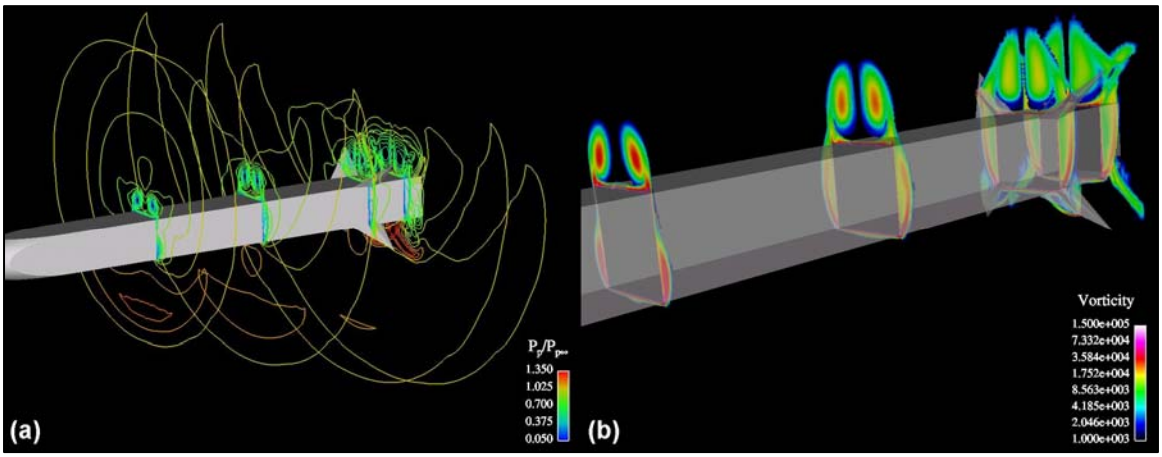

Figure 29. Three-dimensional (a) pitot pressure contours and (b) vorticity contours for corner fin configuration, Mach 2.5, $\phi = 45°$, $\alpha = 14°$.

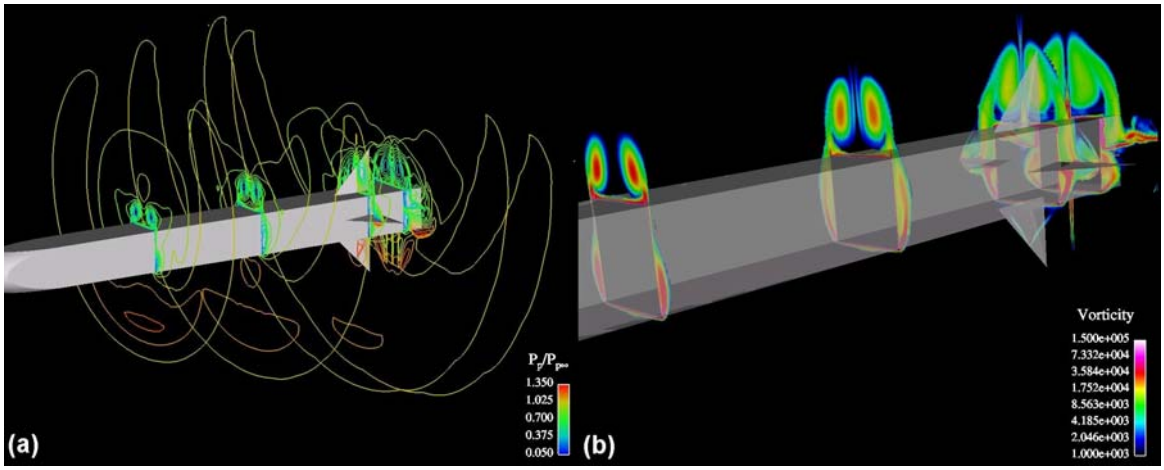

Figure 30. Three-dimensional (a) pitot pressure contours and (b) vorticity contours for side fin configuration, Mach 2.5, $\phi = 45°$, $\alpha = 14°$.

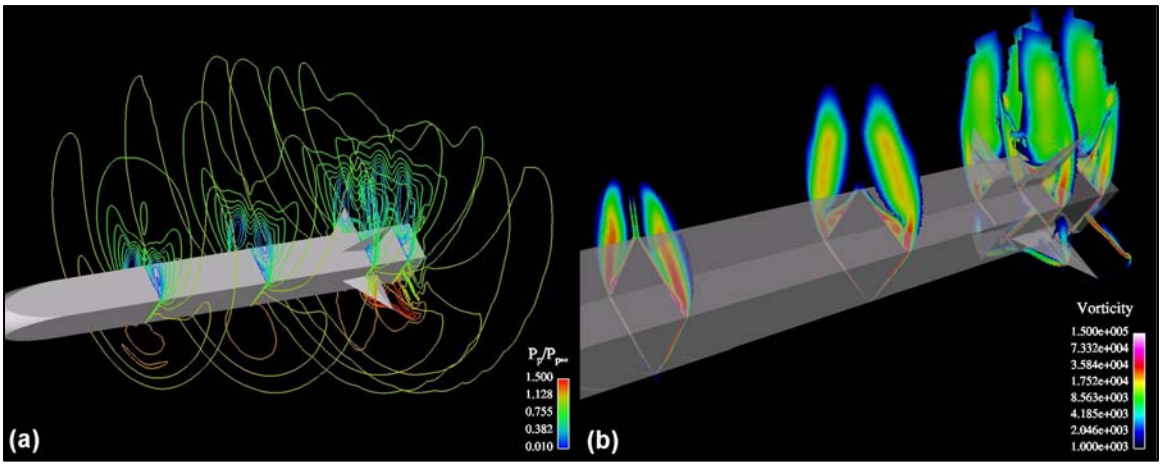

Figure 31. Three-dimensional (a) pitot pressure contours and (b) vorticity contours for side fin configuration, Mach 2.5, $\phi = 0°$, $\alpha = 20°$.

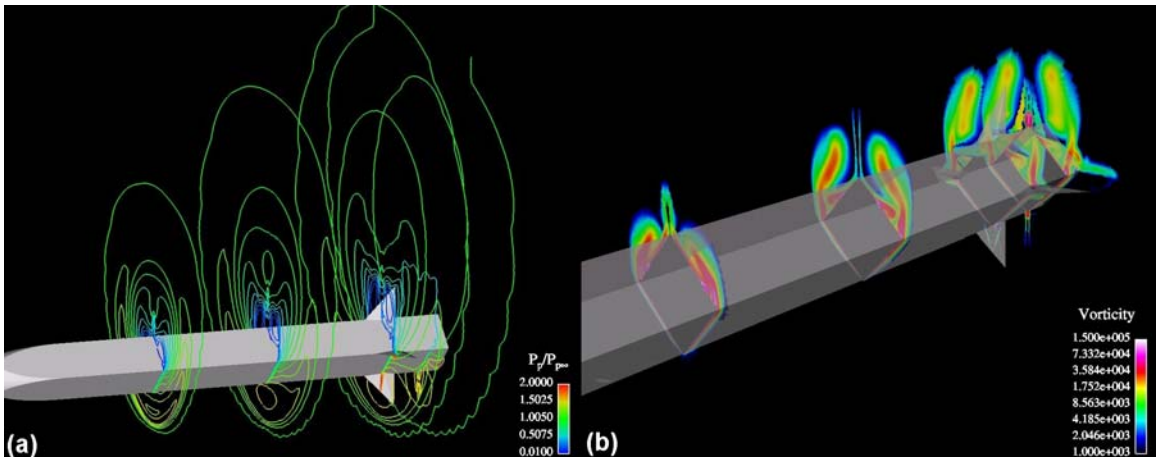

Figure 32. Three-dimensional (a) pitot pressure contours and (b) vorticity contours for corner fin configuration, Mach 4.5, $\phi = 0°$, $\alpha = 14°$.

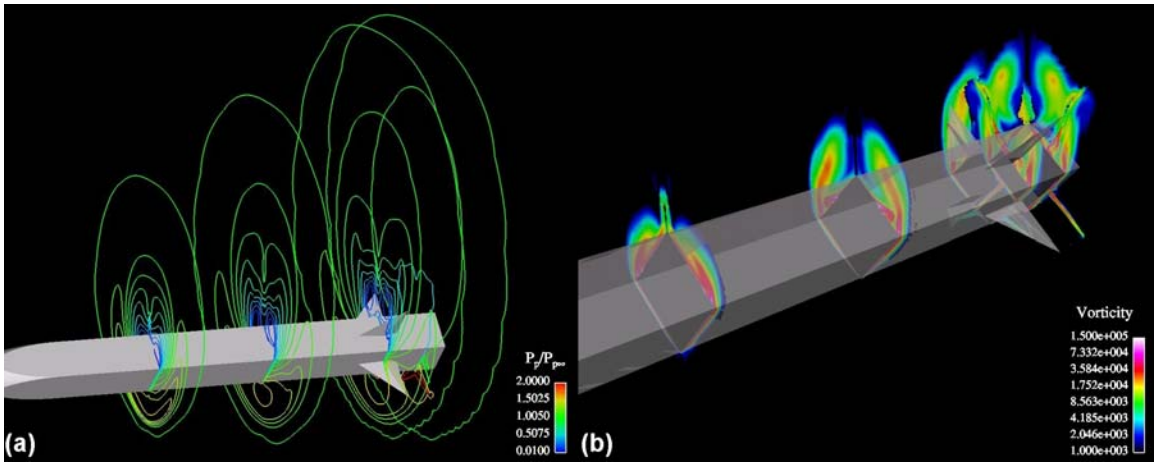

Figure 33. Three-dimensional (a) pitot pressure contours and (b) vorticity contours for side fin configuration, Mach 4.5, $\phi = 0°$, $\alpha = 14°$.

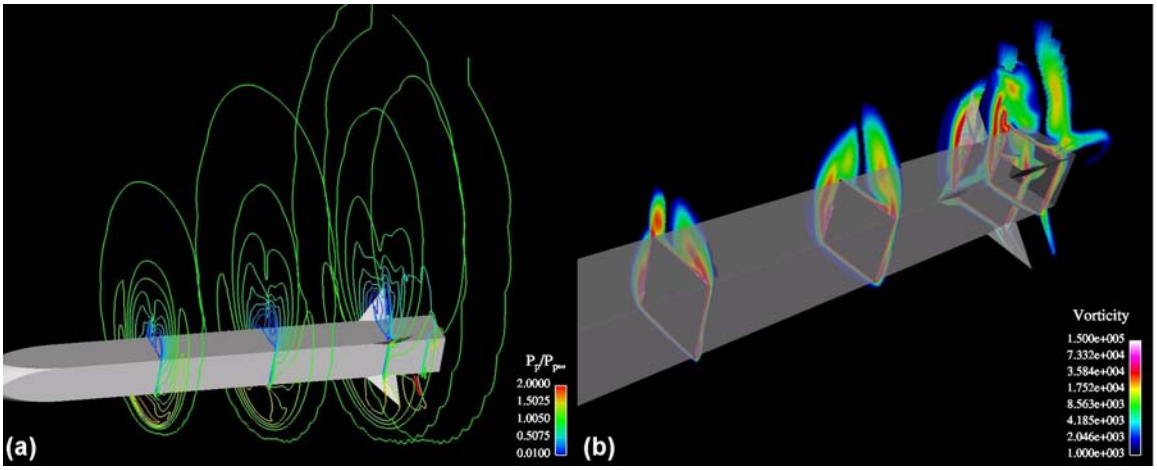

Figure 34. Three-dimensional (a) pitot pressure contours and (b) vorticity contours for corner fin configuration, Mach 4.5, $\phi = 22.5°$, $\alpha = 14°$.

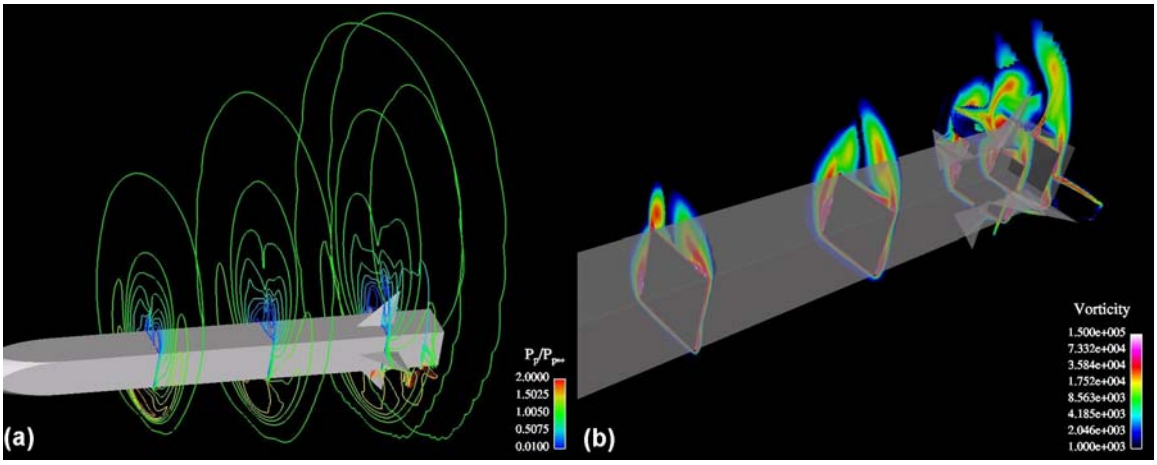

Figure 35. Three-dimensional (a) pitot pressure contours and (b) vorticity contours for side fin configuration, Mach 4.5, $\phi = 22.5°$, $\alpha = 14°$.

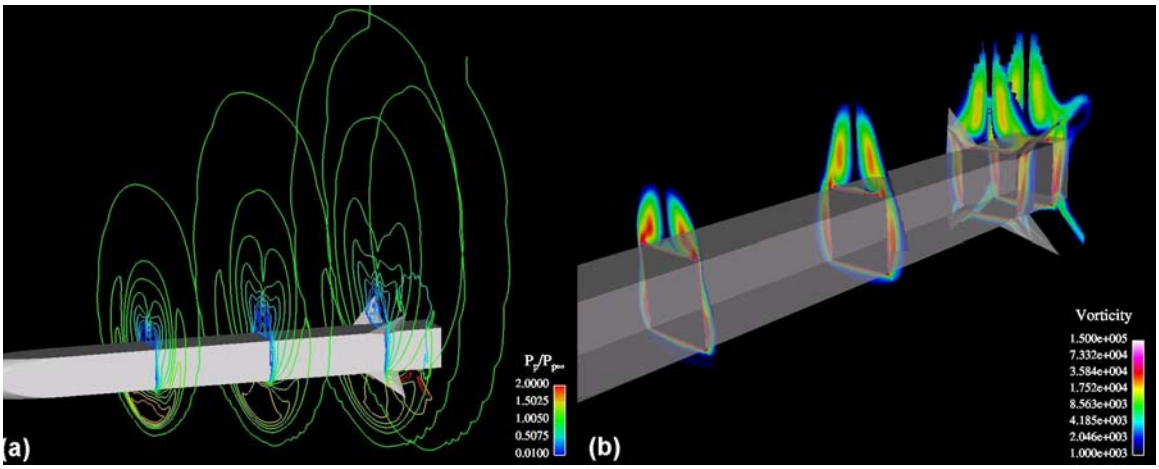

Figure 36. Three-dimensional (a) pitot pressure contours and (b) vorticity contours for corner fin configuration, Mach 4.5, $\phi = 45°$, $\alpha = 14°$.

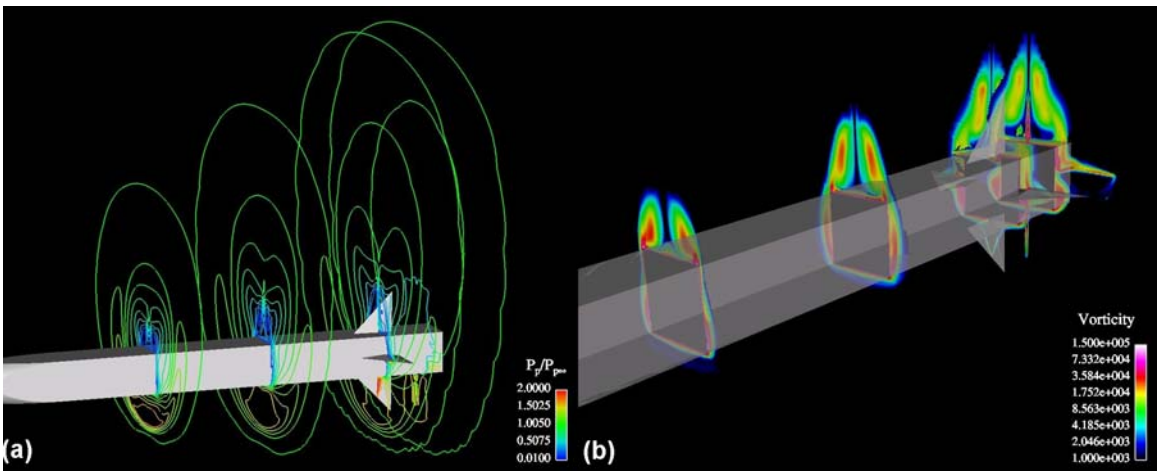

Figure 37. Three-dimensional (a) pitot pressure contours and (b) vorticity contours for side fin configuration, Mach 4.5, $\phi = 45°$, $\alpha = 14°$.

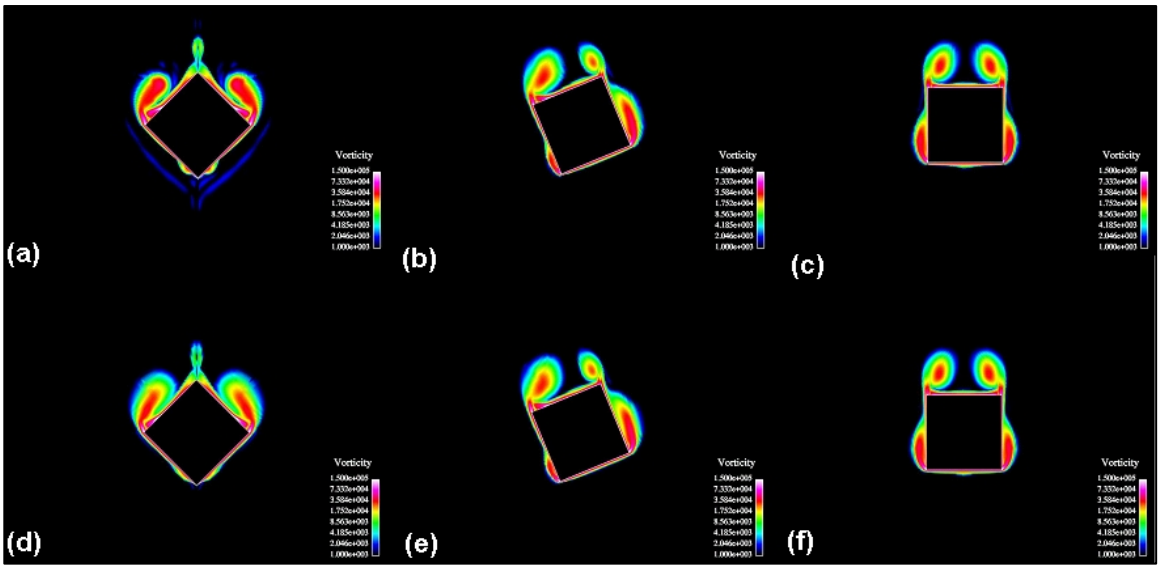

Figure 38. Vorticity contour plots at x/D = 5.5, Mach 2.5, α = 14° for ([a]–[c]) corner fin configuration ϕ = 0°, 22.5°, 45°, respectively, and ([d]–[f]) side fin configuration, ϕ = 0°, 22.5°, 45°, respectively.

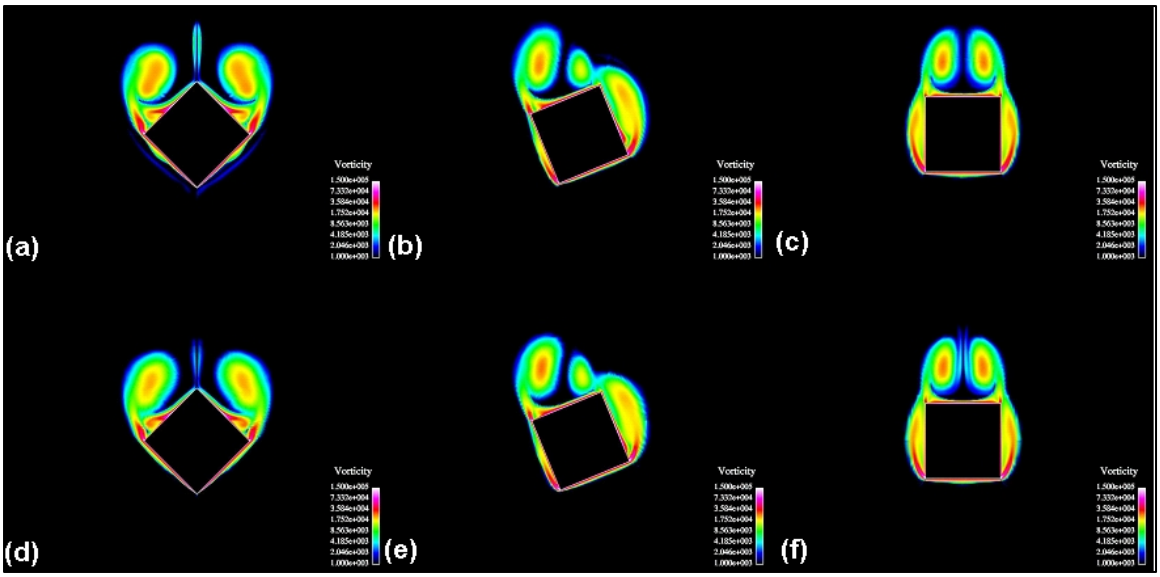

Figure 39. Vorticity contour plots at x/D = 8.5, Mach 2.5, α = 14° for ([a]–[c]) corner fin configuration ϕ = 0°, 22.5°, 45°, respectively, and ([d]–[f]) side fin configuration, ϕ = 0°, 22.5°, 45°, respectively.

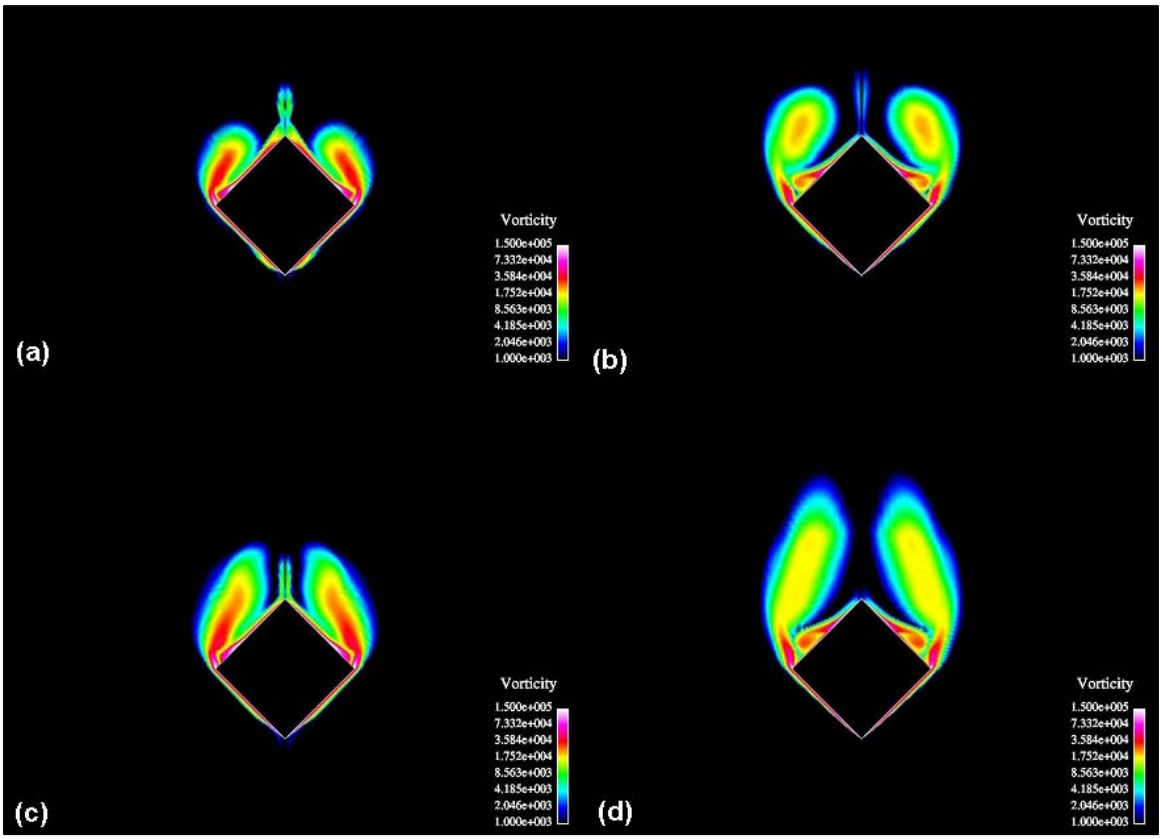

Figure 40. Vorticity contour plots for side fin configuration at Mach 2.5, $\phi = 0°$, ([a]–[b]) $\alpha = 14°$, x/D = 5.5 and 8.5, respectively, and ([c]–[d]) $\alpha = 20°$, x/D = 5.5 and 8.5, respectively.

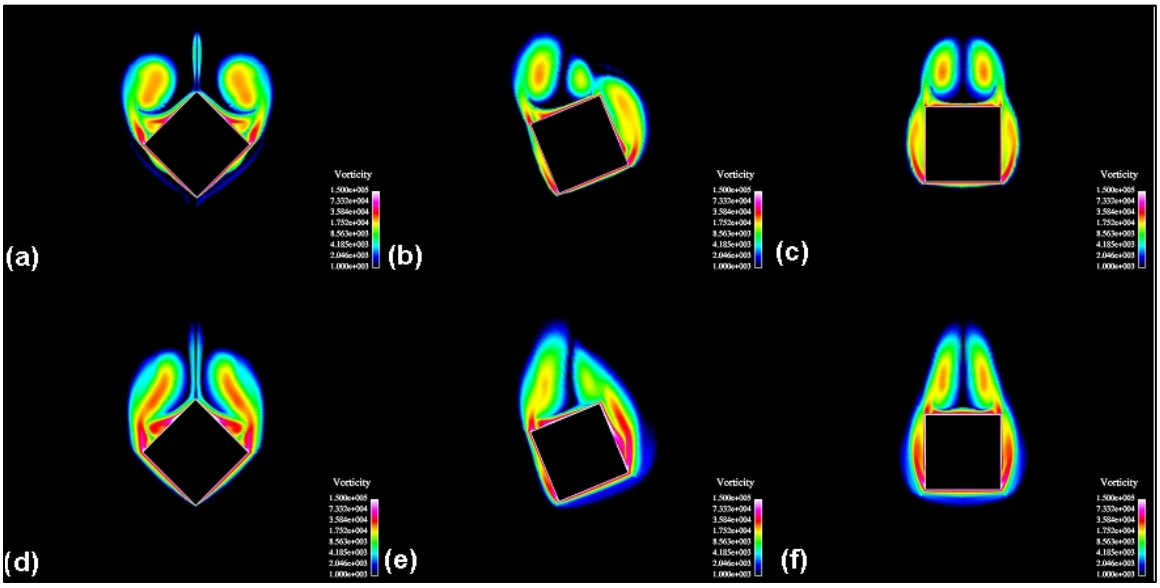

Figure 41. Vorticity contour plots at x/D = 8.5, $\alpha = 14°$ for corner fin configuration ([a]–[c]) Mach 2.5, $\phi = 0°$, 22.5°, 45°, respectively, and ([d]–[f]) Mach 4.5, $\phi = 0°$, 22.5°, 45°, respectively.

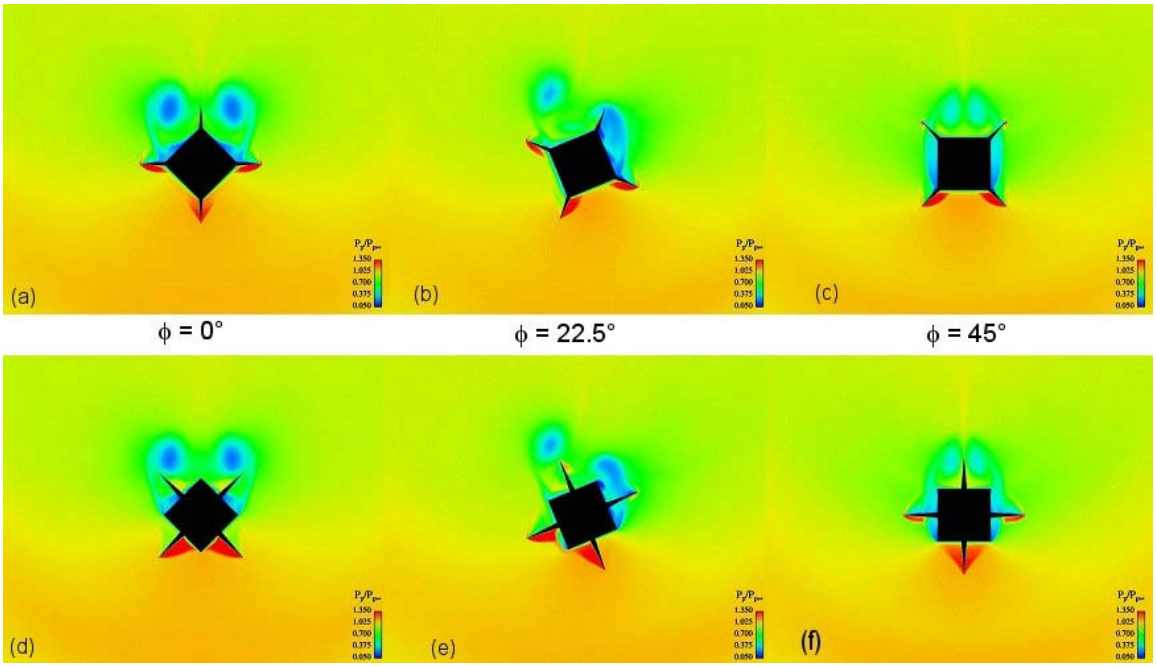

Figure 42. Pressure contours for ([a]–[c]) corner fin configuration and ([d]–[f]) side fin configuration at roll orientations indicated Mach 2.5, α = 14°, x/D = 11.5.

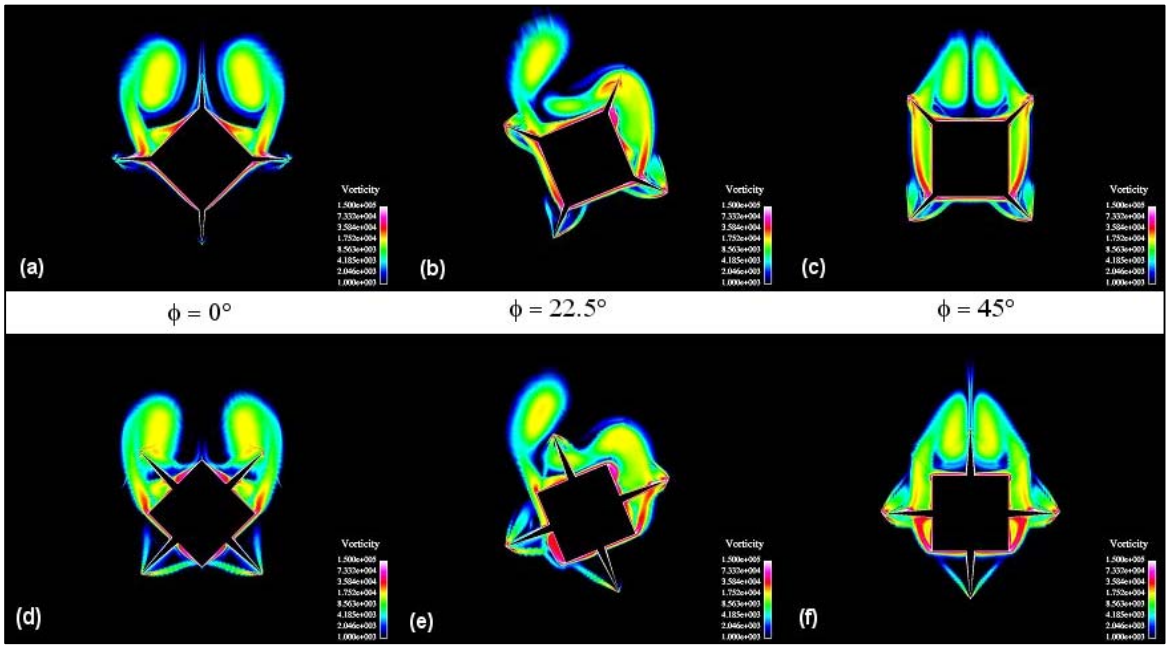

Figure 43. Vorticity contours for ([a] – [c]) corner fin configuration and ([d] – [f]) side fin configuration at roll orientations indicated for Mach 2.5, α = 14°, x/D = 11.5.

Comparing vorticity contours of Mach 2.5 and 4.5 flows for $\alpha = 14°$ at x/D = 11.5 (figure 44) indicates that once again the magnitude of the circulation increases, but the basic vortex structure does not. At x/D = 12.5 (figure 45), the vorticity magnitude as well as the asymmetry for $\phi = 22.5°$ has further increased. At $\phi = 0°$ and $\phi = 45°$, pitch-plane asymmetries do not occur downstream of the fins as the fins themselves are symmetric. Experimental vapor screen images of the corner fin configuration were available for comparison to the computational vorticity contours at x/D = 12.5 and are shown in figure 46 (*17*). The similarities in the vortex cores for all three roll orientations and Mach numbers strongly suggest that the CFD is correctly predicting the flow field for the corner fin configuration. Comparison of the CFD vorticity contours at x/D = 12.5 and the experimental vapor screen images (*17*) for the side fin configuration show similarly good agreement.

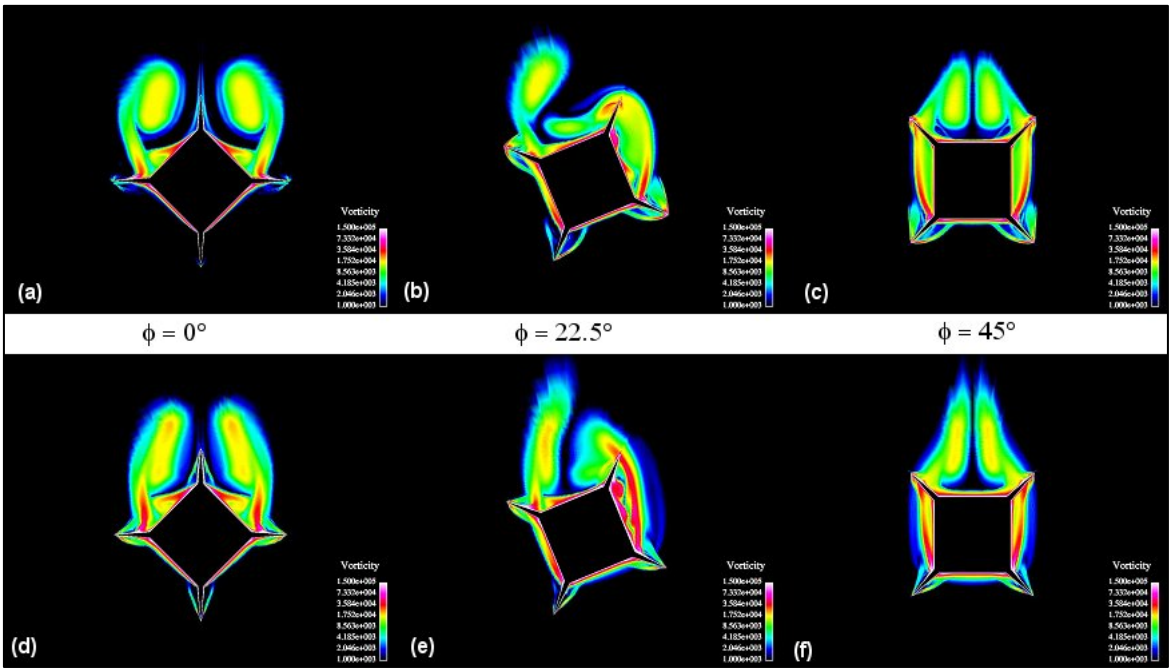

Figure 44. Vorticity contours for corner fin configuration at roll orientations indicated, $\alpha = 14°$, x/D = 11.5 for ([a]–[c]) Mach 2.5 and ([d]–[f]) Mach 4.5.

At both x/D = 11.5 (figure 47) and x/D = 12.5 (figure 48), an increase in α from 14° to 20° for Mach 2.5, $\alpha = 0°$, did not cause the basic vortex structure around most of the projectile to vary, only the sphere of influence. However, the leeward fins cause the vortex cores to become less concentrated at the higher angle of attack as they pass over the fins (figure 47). This disorganization remains apparent as the flow moves downstream of the fins (figure 48b). This indicated that one possible way to increase the aerodynamic forces acting on the fins would be to increase the angle of attack for a given Mach number.

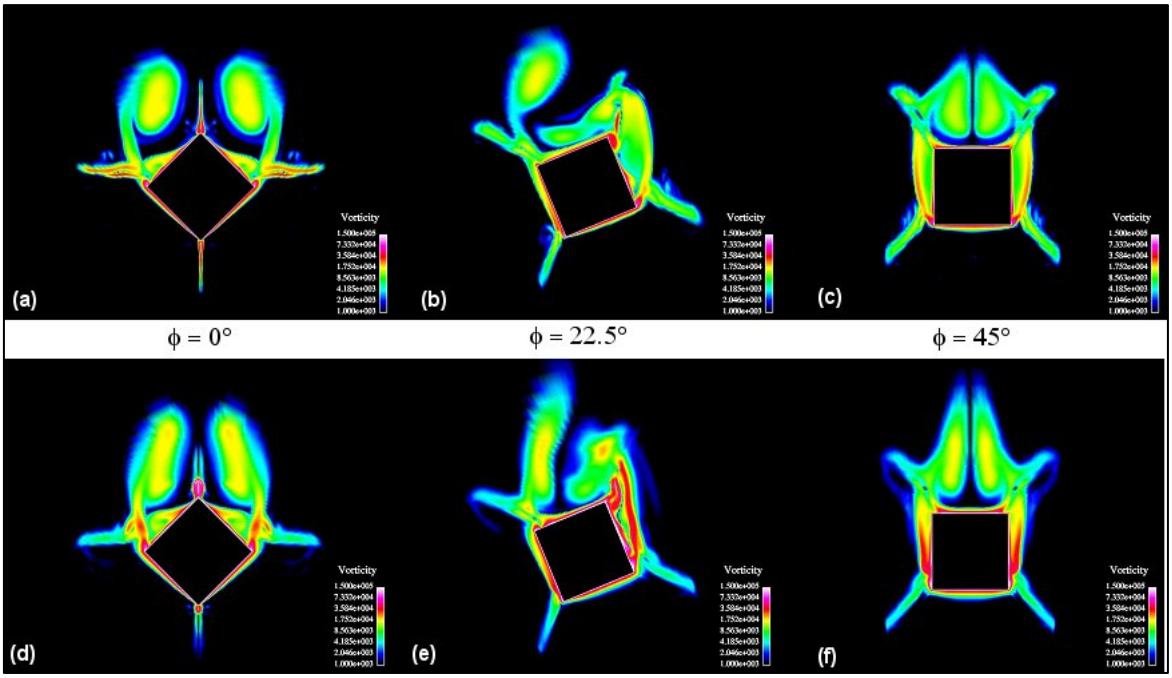

Figure 45. Vorticity contours for corner fin configuration at roll orientations indicated, α = 14°, x/D = 12.5 for ([a]–[c]) Mach 2.5 and ([d]–[f]) Mach 4.5.

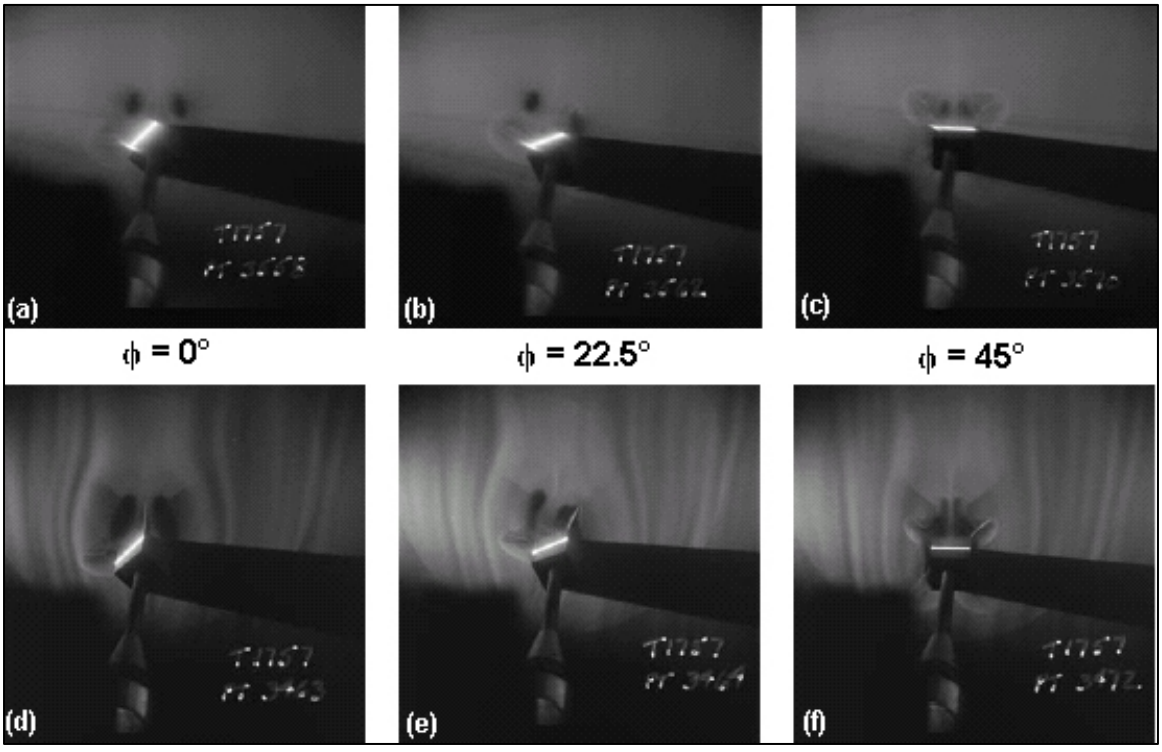

Figure 46. Experimental vapor screen images for corner fin configuration at roll orientations indicated, α = 14°, x/D = 12.5 for ([a]–[c]) Mach 2.5 and ([d]–[f]) Mach 4.5.

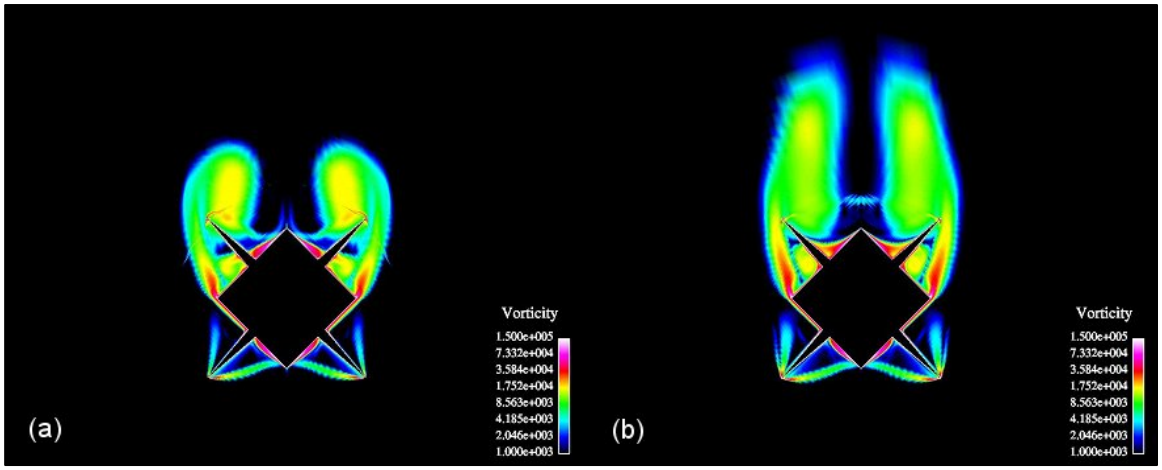

Figure 47. Vorticity contours for side fin configuration at Mach 2.5, $\phi = 0°$, x/D = 11.5, (a) $\alpha = 14°$ and (b) $\alpha = 20°$.

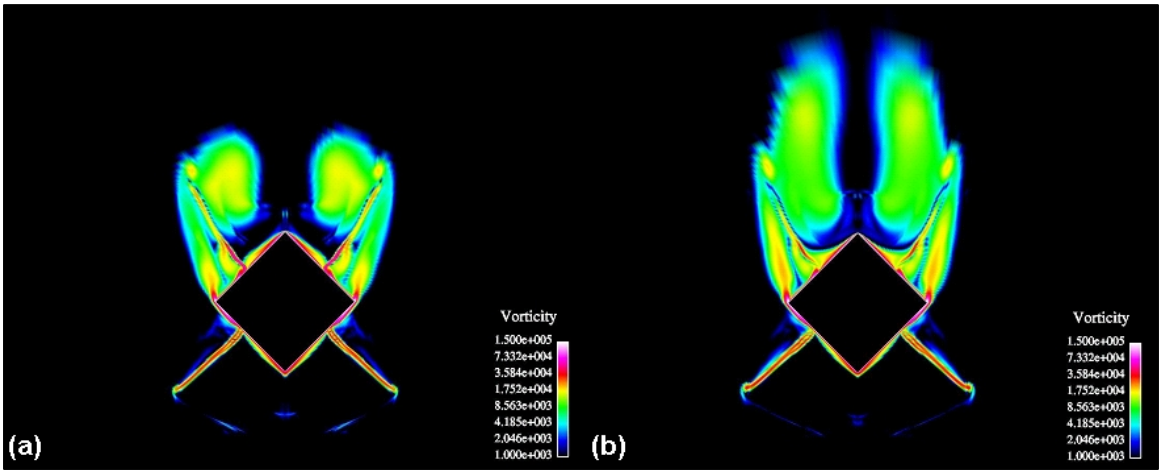

Figure 48. Vorticity contours for side fin configuration at Mach 2.5, $\alpha = 0°$, x/D = 12.5, (a) $\alpha = 14°$ and (b) $\alpha = 20°$.

These changes in the flow field (or lack thereof) explain the similarities and differences seen in the surface pressure distributions. It would appear that a square cross-section missile with pyramid fins, placed either at the corners or on the sides, could be expected to perform quite well. Further studies need to be conducted to determine the dynamic behavior of the projectile before a conclusion could be fully stated.

5. Summary and Conclusions

Numerical computations using viscous Navier-Stokes methods were performed to predict the flow field and aerodynamic coefficients on all missile configurations for wind tunnel test conditions. Full 3-D computations were performed and no symmetry was used. Computational

results were obtained for the square cross-section missile at supersonic speed for various roll orientations and angles of attack using a two-equation k-ε turbulence model. Numerical results show the qualitative features (vortices and cross-flow separation regions) of flow field at various stream wise positions along the missile configurations. Aerodynamic coefficients have been obtained from the computed solutions and found to match well with the available experimental data for these configurations. These numerical results show that modern CFD technique such as the one used in the present computational study is capable of accurately predicting the aerodynamics of complex missile configurations with a square cross section and multiple of fins.

6. References

1. Sahu, J.; Heavey, K. R.; Ferry, E. N. Computational Fluid Dynamics for Multiple Projectile Configurations. *Proceedings of the 3rd Overset Composite Grid and Solution Technology Symposium*, Los Alamos, NM, October 1996.

2. Sahu, J.; Heavey, K. R.; Nietubicz, C. J. Time-Dependent Navier-Stokes Computations for Submunitions in Relative Motion. *6th International Symposium on Computational Fluid Dynamics*, Lake Tahoe, NV, September 1995.

3. Meakin, R. L. Computations of the Unsteady Flow About a Generic Wing/Pylon/Finned-Store Configuration. AIAA 92-4568-CP, August 1992.

4. Pagan, D.; Molton, P.; Delery, J. Basic Experiment on a Supersonic Vortex Flow Around a Missile Body. *Journal of Spacecraft and Rockets* **1992**, *29* (3), 373–378.

5. Grasso, F.; Iaccarino, G. Influence of Crossflow and Turbulence on Vortex Flow Around a Supersonic Missile. *Journal of Spacecraft and Rockets* **1998**, *35* (1), 37–45.

6. Sahu, J.; Heavey, K. R. Application of CFD to High Angle of Attack Missile Flowfields. AIAA Paper No. 2000-4210, *18th Applied Aerodynamics Meeting*, Denver, CO, August 2000.

7. Birch, T.; Wrisdale, I. E.; Prince, S. CFD Predictions of Missile Flowfields. AIAA Paper No. 2000-4211, *18th Applied Aerodynamics Meeting*, Denver, CO, August 2000.

8. Birch, T.; Allen, J.; Wilcox, F. J. Force, Surface Pressure and Flowfield Measurements on Slender Missiles at Supersonic Speeds. AIAA Paper No. 2000-4207, *18th Applied Aerodynamics Meeting*, Denver, CO, August 2000.

9. Edwards, J. A.; Roper, J. J. A Computational Assessment of Static and Dynamic Coefficients for the H3 Hypervelocity Projectile. AIAA Paper 97-0640, January 1997.

10. Orchard, D.; Fournier, E.; Dupuis, A.; Edwards, J. Wind Tunnel Tests on the H3P78, Power Law, Elliptic Section Flared Projectile From Mach 2.5 to 4. AIAA Paper No. 2001-4321, Montreal, Canada, August 2001.

11. Fournier, E.; Orchard, D. *Testing of a Novel Maneuvering Projectile in the DREV Trisonic Wind Tunnel*; technical memorandum report, DREV TM - 2000-108; Canada, July 2000.

12. Edge, H. L.; Clarke, J. *Graphical User Interface for ZEUS*; ARL-TR-1443; U.S. Army Research Laboratory: Aberdeen Proving Ground, MD, June 1996.

13. Edge, H. L.; Sahu, J.; Sturek, W. B.; Pressel, D. M.; Heavey, K. R. *Common High Performance Computing Software Support Initiative (CHSSI) Computational Fluid Dynamics (CFD)-6 Project Final Report: ARL Block-Structured Gridding Zonal Navier-Stokes (ZNSFLOW) Solver Software*; ARL-TR-2084; U.S. Army Research Laboratory: Aberdeen Proving Ground, MD, February 2000.

14. Sahu, J.; Heavey, K. R.; Edge, H. L. Numerical Computations of Supersonic and Hypersonic Flow over Elliptical Projectiles. AIAA Paper No. 2001-4320, Atmospheric Flight Mechanics Conference: Montreal, Canada, August 2001.

15. Orchard, D.; Fournier, E.; Dupuis, A.; Edwards, J. Wind Tunnel Tests on the H3P78, Power Law, Elliptic Section Flared Projectile with Jet Interaction. AIAA Paper No. 2001-4322, Montreal, Canada, August 2001.

16. Sahu, J. Numerical Simulations of Supersonic Flow over an Elliptic-Section Projectile with Jet Interaction. AIAA Paper No. 2002-3260, AIAA Applied Aerodynamics Conference: St. Louis, MO, June 2002.

17. Wilcox, F.; Birch, T.; Allen, J. Force, Surface Pressure, and Flowfield Measurements on a Slender Missile Configuration with Square Cross- Section at Supersonic Speeds. AIAA Paper No. 2004-5451, Applied Aerodynamics Meeting: Providence, RI, August 2004.

18. Peroomian, O.; Chakravarthy, S.; Goldberg, U. A 'Grid-Transparent' Methodology for CFD. AIAA Paper 97-07245, 1997.

19. Peroomian, O.; Chakravarthy, S.; Palaniswamy, S.; Goldberg, U. Convergence Acceleration for Unified-Grid Formulation Using Preconditioned Implicit Relaxation. AIAA Paper 98-0116, 1998.

20. Pulliam, T. H.; Steger, J. L. On Implicit Finite-Difference Simulations of Three-Dimensional Flow. *AIAA Journal* **1982**, *18* (2), 159–167.

21. Goldberg, U. C.; Peroomian, O.; Chakravarthy, S. A Wall-Distance-Free k-ε Model with Enhanced Near-Wall Treatment. *ASME Journal of Fluids Engineering* **1998** *120*, 457–462.

22. ICEM CFD Engineering, ICEM CFD v3.5.1 User's Manual, Berkeley, CA, 2000.

NO. OF
COPIES ORGANIZATION

1 (PDF ONLY) DEFENSE TECHNICAL INFORMATION CTR
DTIC OCA
8725 JOHN J KINGMAN RD
STE 0944
FORT BELVOIR VA 22060-6218

1 US ARMY RSRCH DEV & ENGRG CMD
SYSTEMS OF SYSTEMS INTEGRATION
AMSRD SS T
6000 6TH ST STE 100
FORT BELVOIR VA 22060-5608

1 INST FOR ADVNCD TCHNLGY
THE UNIV OF TEXAS
AT AUSTIN
3925 W BRAKER LN STE 400
AUSTIN TX 78759-5316

1 DIRECTOR
US ARMY RESEARCH LAB
IMNE ALC IMS
2800 POWDER MILL RD
ADELPHI MD 20783-1197

3 DIRECTOR
US ARMY RESEARCH LAB
AMSRD ARL CI OK TL
2800 POWDER MILL RD
ADELPHI MD 20783-1197

3 DIRECTOR
US ARMY RESEARCH LAB
AMSRD ARL CS IS T
2800 POWDER MILL RD
ADELPHI MD 20783-1197

ABERDEEN PROVING GROUND

1 DIR USARL
AMSRD ARL CI OK TP (BLDG 4600)

NO. OF
COPIES ORGANIZATION

1 COMMANDER
NSWC
CODE B40
W YANTA
DAHLGREN VA 22448-5100

1 COMMANDER
NSWC
CODE 420
A WARDLAW
INDIAN HEAD MD 20640-5035

1 AIR FORCE ARMAMENT LAB
AFATL FXA
DAVE BELK
EGLIN AFB FL 32542-5434

3 COMMANDER
US ARMY TACOM ARDEC
AMSTA AR FSF T
BLDG 382
H HUDGINS
J GRAU
W KOENIG
PICATINNY ARSENAL NJ
07806-5000

1 COMMANDER
US ARMY TACOM
AMSTA AR CCH B
P VALENTI
BLDG 65S
PICATINNY ARSENAL NJ
07806-5001

1 COMMANDER
US ARMY ARDEC
SFAE FAS SD
J HEDDRICTL
PICATINNY ARSENAL NJ
07806-5001

1 NAWC
D FINDLAY
MS 3 BLDG 2187
PATUXENT RIVER MD 20670

1 UNIV OF ILLINOIS AT URBANA
CHAMPAIGN
DEPT OF MECHANICAL AND
INDUSTRIAL ENGRNG
J C DUTTON
URBANA IL 61801

NO. OF
COPIES ORGANIZATION

1 COMMANDER
US ARMY TACOM-ARDEC
BLDG 162S
AMCPM DS MO
P BURKE
PICATINNY ARSENAL NJ
07806-5000

ABERDEEN PROVING GROUND

19 DIR AMSRD ARL
AMSRD ARL WM
J SMITH
AMSRD ARL WM B
T KOGLER
W CIEPIELA
AMSRD ARL WM BA
D LYON
AMSRD ARL WM BD
B FORCH
AMSRD ARL WM BC
P PLOSTINS
J DESPIRITO
B GUIDOS
K HEAVEY (3 CPS)
J NEWILL
J SAHU
S SILTON
P WEINACHT
AMSRD ARL WM BF
S WILKERSON
H EDGE
AMSRD ARL SL BE
A MIKHAIL
AMSRD ARL CI HC
R NOAK

NO. OF
COPIES ORGANIZATION

1 J EDWARDS
MCM DEPARTMENT
DSTL FORT HALSTEAD
SEVEN OAKS
KENT NT14 7BP
UK

INTENTIONALLY LEFT BLANK.